

Fluctuations above a burning heterogeneous propellant

L. MASSA, T. L. JACKSON, J. BUCKMASTER[†]
AND F. NAJJAR

Center for Simulation of Advanced Rockets, University of Illinois at Urbana-Champaign,
1304 West Springfield Avenue, Urbana, IL 61801, USA

(Received 18 September 2005 and in revised form 15 November 2006)

A numerical description of heterogeneous propellant combustion enables us to examine the spatial and temporal fluctuations in the flow field arising from the heterogeneity. Particular focus is placed on the fluctuations in a zone intermediate between the combustion field (where reaction is important) and the chamber flow domain, for these define boundary conditions for simulations of the turbulent chamber flow. The statistics of the temperature field and the normal velocity field are described, and characteristic length scales and time scales are identified. The length scales are small compared to any relevant length scale of the chamber flow, and so the boundary conditions for this flow at any mesh point are statistically independent of those at any other mesh point. But the temporal correlations at a fixed point are significant, and affect the nature of the chamber flow in a variety of ways. We describe the fluctuations in the head-end pressure that arise because of them, and contrast these results with those calculated using a white-noise assumption.

1. Introduction

Consider the numerical simulation of a rocket-motor chamber flow. This is a problem whose solution is important in rocket design, and in the study of safety scenarios. It is also a difficult problem, a challenge to the most advanced computing resources of the day. For example, at the Center for Simulation of Advanced Rockets (CSAR) at the University of Illinois[‡] a code has been constructed to simulate the flow in the solid-propellant boosters of the Space Shuttle (Fiedler *et al.* 2005; Fiedler, Wasisto & Brandyberry 2006) and, running on the US Department of Energy's most powerful computers, only 600 milliseconds or so of physical time can be simulated. Short though this is, however, particularly in comparison with the 2 minute burn-out time of the boosters, ignition transients and certain accident scenarios can be studied. Calculations for longer time periods can be carried out for rockets that are much smaller than the boosters.

The code accommodates turbulence using large-eddy simulations (Wasisto, Balachandar & Moser 2004; Wasisto & Moser 2005). Here a new challenge, not present in traditional scenarios, is a proper accounting of the nature of the injected flow at the chamber/propellant boundary. Particularly for heterogeneous propellants,

[†] Author to whom correspondence should be addressed: Buckmaster Research, 2014 Boudreau Drive, Urbana, IL 61801, USA, limey@uiuc.edu

[‡] www.csar.uiuc.edu

this flow and the vorticity it carries is neither steady nor spatially uniform. These fluctuations could well have an effect on the overall chamber flow and, indeed, there is a significant amount of experimental and computational work that demonstrates the effect of perturbations of initial or boundary conditions on the long-time or far-field solution of turbulent flow fields (Moser, Rogers & Ewing 1998). Also, of particular interest in rocket flows is the interaction between the omnipresent acoustic waves and fluctuations of the injected flow, and a number of studies have shown how important this can be for certain parameter values (Zhao *et al.* 2000; Flandro 1986). (It is worth noting, for the reader unfamiliar with solid-propellant rockets, that because of the large efflux velocities there is no boundary layer above the burning propellant. These flows – interior flows generated by wall injection – are of the kind first studied by Taylor (1956). See also Proudman (1962), Culick (1966), Balachandar, Buckmaster & Short (2001). Inviscid flows of this kind are rotational and satisfy the no-slip condition at the injection surface without benefit of viscosity. The large-eddy simulations of compressible rocket flow reported in Wasisto *et al.* (2004) yield solutions with means that agree well with the compressible version of Taylor flow reported in Balakrishnan, Linan & Williams 1991.)

For these reasons alone, notwithstanding the significance of any findings, it is of interest to describe the nature of the flow field at an intermediate distance above the propellant surface, intermediate in the sense that the distance is large compared to the scale of the flame structure, but small compared to appropriately defined flow scales. In order to do this it is necessary to have a code that can simulate heterogeneous propellant combustion, and in recent years such a code has been developed and refined as part of the Space Shuttle study (Jackson & Buckmaster 2002; Massa *et al.* 2002; Massa, Jackson & Buckmaster 2005). It has a number of ingredients.

The propellant itself, typically restricted to ammonium perchlorate (AP) in binder, is modelled by representing the AP particles by spheres. The sizes of the spheres can be chosen to match the size distribution of industrial packs (Kochevets *et al.* 2001). Within the propellant, heat conduction is accounted for, with different conductivities for the two components. AP particles that are too small to be resolved numerically are accounted for using a homogenization strategy (Chen *et al.* 2002).

The processes occurring in the neighbourhood of the propellant surface – melting, heterogeneous reaction, etc. – are accounted for using simple pyrolysis laws relating the surface regression rate to the surface temperature. Different parameters are required for the different components, and here also a homogenization strategy is used to accommodate the smallest AP particles (Chen *et al.* 2002).

When aluminum is not present, the surface can be represented by a single-valued function provided that it has no unusual topographical features, such as cracks. Then its evolution is governed by a simple first-order equation of the Hamilton–Jacobi type.

Finally, in the gas phase, the variable-density low-Mach-number reactive Navier–Stokes equations are solved. Either a two-step kinetics model is used, or a three-step model. Each step of the latter corresponds to a single flame of the familiar Beckstead–Derr–Price model of heterogeneous propellant combustion (Beckstead, Derr & Price 1970).

Validation of the overall code is discussed in Massa *et al.* (2005), and its application to the acoustic response of burning propellant is reported in Buckmaster *et al.* (2005). In this past work it has not been necessary to integrate away from the surface more than a few hundred microns, since the burning rate is not affected by the flow beyond that zone. Here it is necessary to examine the combustion field on the millimetre scale.

Diameter	Number of Spheres
567.450	1
520.350	12
477.150	24
437.550	74
401.250	213
367.950	465
337.400	935
309.400	1450
283.700	2111
260.650	2917
239.050	3717
218.750	4641
200.600	5126
183.950	5748
168.700	6159
154.700	6027
141.850	5907
130.100	5675
119.300	5440
109.400	5030
100.330	4941
91.980	4701
84.350	4584
77.350	4727
70.930	4551
65.045	4738
59.645	5330
54.695	4756

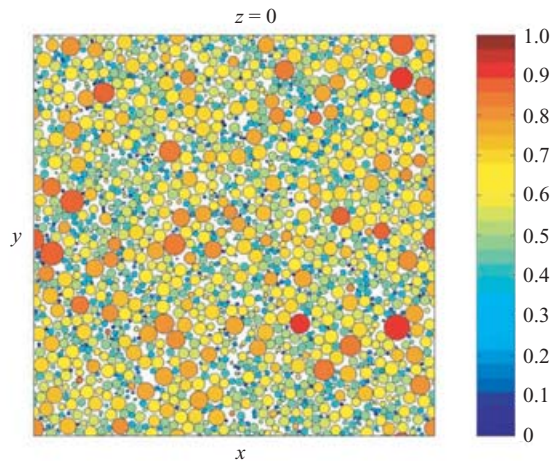


FIGURE 1. A slice through a typical pack generated by the packing code. The packs are periodic in all three directions. Colour scale denotes scaled particle size.

The structure of the paper is as follows. In §2 we briefly describe the coupled combustion code on which the present work is built, and the evidence we have that it reflects reality to some degree. In §3 we describe the various propellant morphologies for which the calculations are carried out. The gas-phase fluctuations generated by the combustion of these propellants evolve as distance from the surface increases, and this evolution is described in §4. Section 5 is concerned with the fluctuation statistics, and the associated length scales and time scales. And §6 describes the chamber flow analysis.

2. The coupled combustion code

The combustion code simulating the gas-phase combustion field and the heat conduction within the solid propellant, coupled via the regressing propellant surface, is described in Jackson & Buckmaster (2002) (two dimensions) and Massa *et al.* (2002, 2005) (three dimensions). Details of the numerical strategies, along with verification studies, are reported in Massa, Jackson & Short (2003). Readers interested in the issue of parameter choices should refer to Massa *et al.* (2002, 2005); those interested in experimental validation, Massa *et al.* (2005); those in verification, Massa *et al.* (2003). Here we briefly describe the equations and the numerical strategies adopted to ensure accuracy.

A key ingredient is a model of the propellant morphology, one that is generated using a sphere-packing code (Kochevets *et al.* 2001; Knott, Jackson & Buckmaster 2001), and a slice through a typical model pack is shown in figure 1.

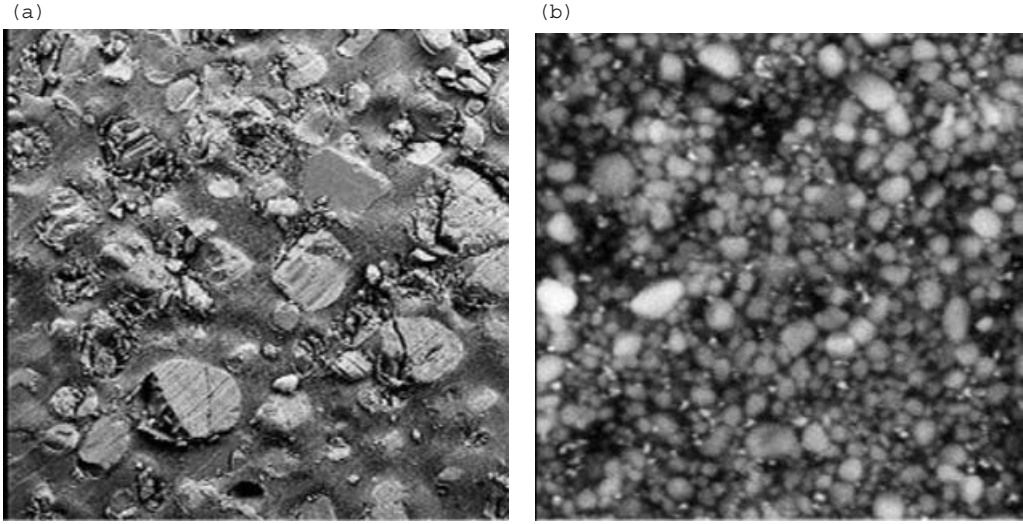


FIGURE 2. Photomicrographs of a laboratory bimodal pack (courtesy of Q. Brewster): (a) particles of order 200 microns in diameter, (b) of order 2 microns.

It is typical of industrial packs that the AP particles range in size from $\sim 1 \mu\text{m}$ to $\sim 100 \mu\text{m}$.; figure 2 shows two photomicrographs of a laboratory pack with this characteristic. Note that real AP particles are not spheres, but we have reason to believe, from a study of spheroid packs (Wang, Jackson & Buckmaster 2007b), that this is of no concern provided the particle distribution is statistically isotropic.

It is unrealistic to expect that the combustion code can both resolve the $\sim 1 \mu\text{m}$ particles and, at the same time, accommodate the $\sim 100 \mu\text{m}$ particles. And a significant volume fraction of AP could be unresolvable thereby, and its role cannot be neglected. For this reason we have developed homogenization strategies in which the finest AP particles are blended with the fuel binder and the required properties of this blend are calculated (Chen *et al.* 2002).

Heat conduction within the solid is governed by

$$\rho_s c_s \frac{\partial T}{\partial t} = \nabla \cdot (\lambda_s \nabla T) \quad (1)$$

where T is the temperature, ρ_s is the density, c_s the specific heat, and λ_s the conductivity. ρ_s and λ_s are assigned different values according to whether they are located in pure AP or in AP/binder blend. The discontinuity in λ_s at the particle boundaries implies that the temperature gradient is discontinuous there, and so a well-established but non-classical finite-difference strategy is adopted, Massa *et al.* (2002). This was tested on one-dimensional problems with analytical solutions. Because the multi-scale aspects of the problem are eliminated by the homogenization strategy, a uniform mesh suffices provided it is fine enough to accommodate the smallest particles that are not homogenized. The solution of test problems with Dirichlet data at the top and bottom boundaries, and periodicity conditions at the side boundaries, shows that at least 10 mesh points are required across a particle diameter.

The propellant surface moves in a highly irregular unsteady fashion, and it is convenient to fix it in the computational frame. This is possible provided it can be described by the single-valued function f :

$$\eta = f(\xi, \zeta, t) \quad (2)$$

where η is measured normal to the surface (nominally), and ξ, ζ parallel to the surface (nominally). Then, in the field equations η can be replaced by $y = \eta - f$, the height above or below the surface, fixed at $y=0$. If the normal regression speed of the surface is r_b , f satisfies the equation

$$f_t + \sqrt{1 + f_\xi^2 + f_\zeta^2} = 0 \quad (3)$$

and this is solved using a WENO scheme; r_b is related to the surface temperature by a simple pyrolysis law

$$r_b = A \exp(-B/T) \quad (4)$$

where A and B take on different values in the two different materials. The pyrolysis law, commonly used, subsumes complex and poorly understood physics that occurs at and just below the surface.

A method of testing the accuracy of the WENO scheme, which we used, is to choose a function f and add a forcing term to the right-hand side of (3) so that the choice is a solution of the modified equation. An approximation to f is then generated by integration, for comparison with the exact function.

The mapping function defined here which defines y , a computational variable, is the simplest choice using f and is adopted in all of our earlier work. A slight modification, to be described later, is used in the present work.

The gas-phase combustion field is described by the incompressible (but variable-density) Navier–Stokes equations (momentum and mass conservation), the small-Mach-number energy (temperature) equation, and equations for the reactants. The latter have the form

$$\rho c \frac{DT}{Dt} = \nabla \cdot (\lambda \nabla T) + q, \quad \rho \frac{DY_i}{Dt} = \nabla \cdot (\rho D_i \nabla Y_i) - \alpha_i, \quad (5)$$

where q is the heat generated by the reactions (each an Arrhenius function of T) and α_i is the rate at which the reactant Y_i is consumed by the reactions. D_i is the diffusion coefficient.

A detailed discussion of the numerical strategies used for the integrated problem (solid, interface, gas) can be found in Massa *et al.* (2003), together with algorithm verifications and accuracy tests. Overall, the accuracy is second-order both in time and space. Application of the code, with a discussion of the parameter choices, is described in Jackson & Buckmaster (2002) and Massa *et al.* (2002, 2005).

The computational challenges of this problem, which should always be borne in mind, preclude accommodation of real chemical kinetics. Rather, we use global kinetics with either 2 or 3 steps. The 3-step model comprises: an AP decomposition flame; the so-called primary diffusion flame in which AP pyrolysis gases react with binder pyrolysis gases; and the so-called secondary diffusion flame in which the products of the AP decomposition react with binder pyrolysis gases. For the 2-step model the primary diffusion flame is neglected.

The choice of parameters, of which there is a large number, presents a serious challenge. For some, the experimental examination of subcomponents of the problem has yielded data of varying reliability. This is true, for example, for the pyrolysis rate parameters and those that define the energetic consequences of the pyrolysis.

As creatures of false kinetics, the kinetics parameters cannot be determined by a chemist's wizardry, but can only be deduced from burning-rate measurements and related measurements such as those of the sensitivity of the burning rate to the propellant supply temperature. The danger here is that the whole endeavour will

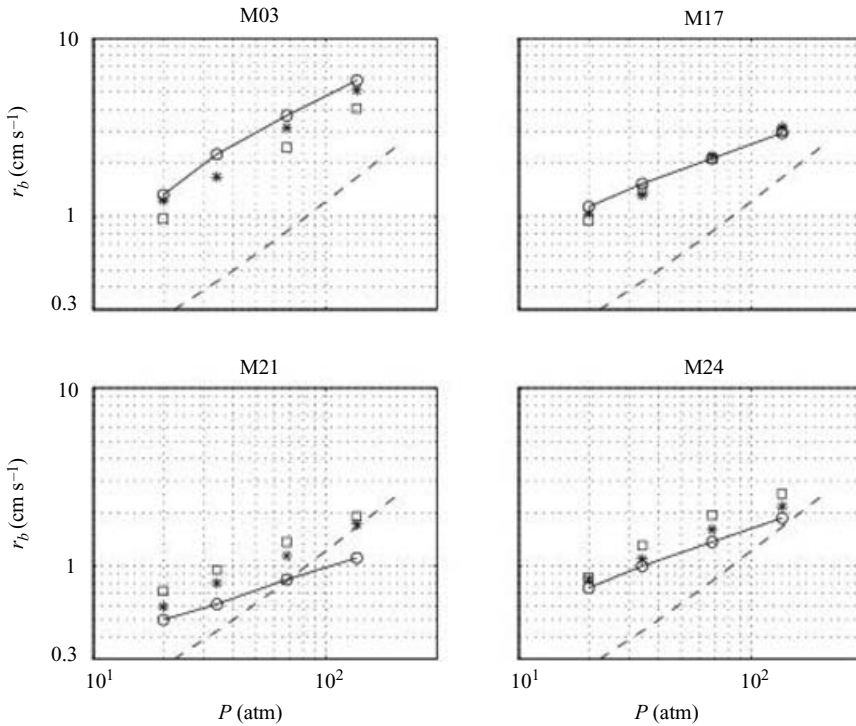


FIGURE 3. Burning rates for various Miller packs: experimental (joined circles) and numerical (squares: 2-step kinetics; asterisks: 3-step kinetics). The dashed line is the burning rate of pure AP.

degenerate to one of elaborate curve-fitting, of limited value. For this reason we have been particularly careful to avoid the use of three-dimensional burning-rate data, and have used only one-dimensional data, the burning rates of pure AP or of fine AP/binder blends. Then predictions of three-dimensional burning-rate variations with propellant morphology can be used for validation.

Unfortunately, few data are available for such purposes; indeed, all that we are aware of are reported in Miller (1982). There, Miller describes the statistics for a number of packs, together with their burning rates over a range of pressures. Figure 3 shows comparisons between these data and the numerical predictions for four such packs; the numerical results are calculated using either the 2-step or the 3-step chemistry model. Note that at the highest pressure the measured burning rate for M03 is approximately 6 cm s^{-1} , and for M24 it is a little under 2 cm s^{-1} : There are significant morphology effects.

An examination of the results for M03 shows excellent agreement when 3-step kinetics is used, except for $P = 34 \text{ atm}$. This is a pack for which a substantial amount of homogenization of fine AP is required, and at $P = 34 \text{ atm}$ the one-dimensional blend displays a pulsating instability. Such instabilities are not surprising, but the conditions for which they occur are controlled by the choice of kinetics parameters, and there is no reason to believe that they coincide with the experimental ones. Thus the discrepancy noted here merely draws attention to the fact that the strategy used in Massa *et al.* (2005) to fit the kinetics parameters should be modified to incorporate stability criteria. Efforts are under way to accomplish this.

Name	Particle distribution cuts	Particle number	D_{max} (μm)	D_{min} (μm)	$\alpha_V : \alpha_H$	$L_x = L_z$ (mm)	grid $n_x \times n_z \times n_y$
H200	200 μm 100 %	8×10^3	200	200	62:0	3.78	$180 \times 180 \times 67$
Th200	Th200 100 %	1×10^4	458	50	64:41	3.247	$191 \times 191 \times 67$
P82	P82 100 %	3×10^4	89	75	61:46	2.22	$191 \times 191 \times 67$
P82_390	P 82 20 % P390 80 %	3×10^4	401	72	69:0	3.8	$191 \times 191 \times 67$
Th20_50_200	Th20 16 % Th50 48 % Th200 36 %	2×10^4	404	40	70:0	1.93	$151 \times 151 \times 67$

TABLE 1. Summary of the propellant morphologies. In the sixth column, α_V is the volumetric fraction (percent) of oxidizer spheres in the pack, while α_H is the volumetric fraction of binder that is actually oxidizer (homogenization). The total volume fraction of oxidizer is $\alpha_T = \alpha_V(1 - \alpha_H) + \alpha_H$. In the seventh column, L is the side of the x, z sections of the pack. In the eighth column, the same grid is used in both solid and gas phase; the value reported refers to one phase only.

For M17, both the 2-step and the 3-step model yield excellent agreement; for M24, as for M03, the 2-step model is inadequate, but the 3-step model works well; and for M21 it would appear that neither model is satisfactory. However, there is reason to question the experimental data for M21. Each panel in figure 3 shows a dashed line that defines pure AP burning rates, and we see that for M03, M17, and M21 these rates lie below those of the heterogeneous propellant. Moreover, there are indications that the rates converge at high pressures for M17 and M24 (particularly for the latter) and it has long been argued that this is a universal expectation. On the other hand, for M21 the measured heterogeneous rates drop below the AP rates at high pressures. For this reason, and in the absence of confirmation of the M21 data, we report this discrepancy but are little concerned by it.

To conclude. The problem is a complex one that cannot be dealt with by rational approximations to exact ingredients; rather, a significant number of component models must be adopted, many of which can be legitimately criticized. But the successful comparisons of figure 3 provide some support to the idea that the code can be usefully applied to scientific issues of propellant combustion that go deeper than the mere calculation of burning rates. The acoustics study of Buckmaster *et al.* (2005) is an example; the calculation of far-field perturbations that we present here is another.

3. The propellant morphology used in calculating the fluctuations

The object of this paper is to learn something of the nature of the fluctuations in the flow field generated by the combustion of a heterogeneous propellant. Such fluctuations will be strongly influenced by the propellant morphology, and we shall consider five different morphologies, some of the fundamental parameters of which are shown in table 1. Here, in the names in the first column, 'P' marks a pack that represents a morphology studied by Sambamurthi, Price & Sigman (1984), and 'Th' marks a pack that represents a morphology studied at ATK Advanced Launch Systems (formerly ATK Thiokol Corporation).

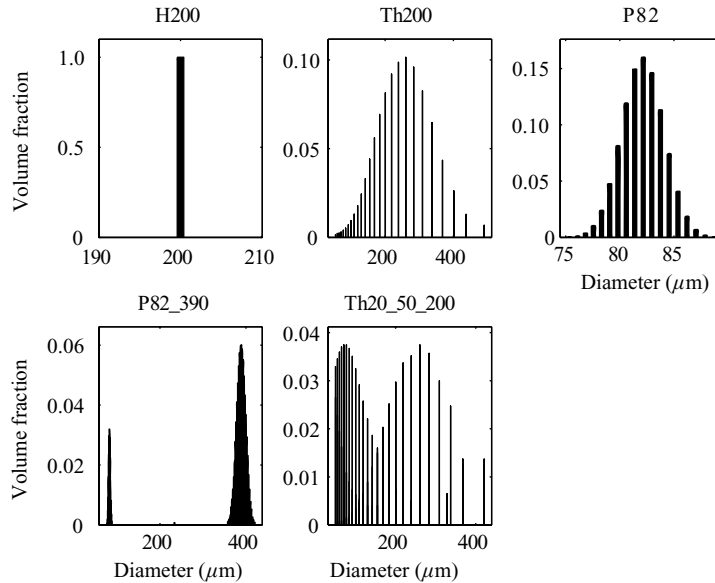


FIGURE 4. Particle size distribution for the five packs described in table 1.

H200 is a monomodal pack, one in which all of the particles have the same diameter. Eight thousand particles are packed in a cube of side 3.5 mm. The packing fraction α_V , the percentage of cube volume occupied by the spheres, is 62 %, and there is no oxidizer homogenized into the binder, so that α_H is zero. In general, the ‘binder’, the volume of the cube external to the spheres, is a blend of fuel and homogenized oxidizer.

Th200 is a Thiokol distribution in which the spheres range in diameter from 50 μm to 458 μm , and 41 % of the binder is oxidizer, so that with 64 % of the total volume occupied by spheres, 78.76 % of the total volume is oxidizer. The size distribution is shown in figure 4.

The data for P82 can be understood in the same way as those for Th200. And P82_390 is simply a combination of two distributions, P82 and P390, in the proportion of 20 to 80. Similarly, Th20_50_200 is a combination of three distributions. Slices through the various packs are shown in figure 5; note that they are not drawn to scale.

It is, we believe, of interest to compare the solutions for H200 (mono-modal) with those of Th200 (a single distribution with particles of similar mean size). And comparing Th200 with P82 gives an indication of the effects of mean size for single distributions. The packs P82_390 and Th20_50_200 are characterized by multiple distributions more characteristic of those used in practice.

4. The fluctuations and their evolution

The issue of fluctuations (both spatial and temporal) in the burning of a heterogeneous propellant, and their relationship to the fluctuations in the chamber flow, is a complicated one. Fluctuations arising from the heterogeneity occur at the propellant surface and evolve as they are convected away from the surface. That they are non-trivial is suggested by recent photographs taken at China Lake, figure 6. It is natural to ask if they eventually influence the turbulent chamber flow, and this is a

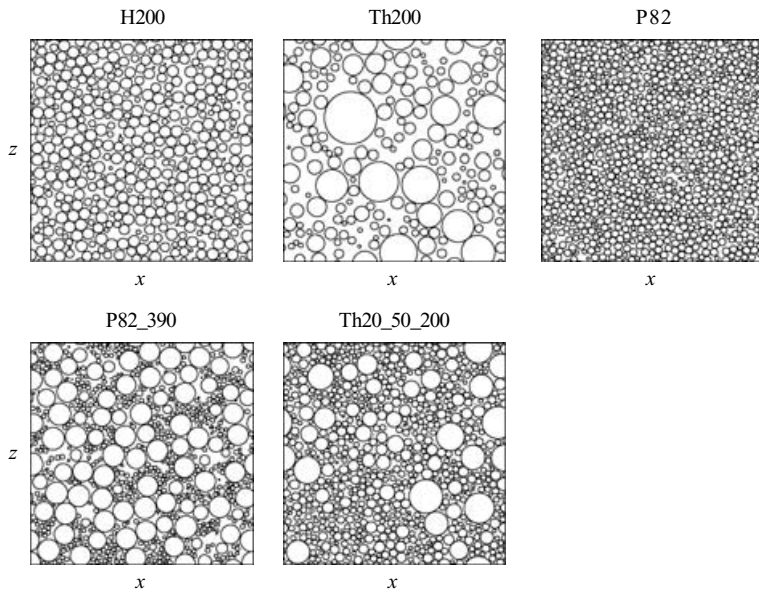


FIGURE 5. x, z sections of the five packs described in table 1 (not to scale).

question that can be addressed using the combustion code described in §2, together with chamber-flow simulations. At the same time, it has long been understood that near-wall velocity fluctuations (turbulent eddies) can penetrate the combustion field and affect the burning rate, leading to what is known as erosive burning, Landsbaum (2005), although the precise nature of erosive burning has never been adequately described. Also, in cases where the local Mach number of the flow is not small, local pressure fluctuations associated with the velocity fluctuations could be large enough to affect local burning rates; local Mach numbers are not small near the nozzle end of large rockets. And temporal fluctuations of the mean chamber pressure can affect the mean burning rate throughout the chamber.

The simulation of this fully coupled problem is not something that we yet know how to do. Indeed, the problem of erosive burning by itself is of this nature. Instead, we ignore all effects of chamber fluctuations on the burning rate. In this connection it is worth noting that erosive burning is unimportant if the chamber flow velocity is not large, as near the fore end of the chamber, or for a small rocket. But as with any complex two-way coupled problem, legitimate scientific enquiry includes the analysis of each one-way component. It could be the case, for example, that all fluctuations associated with the heterogeneity occur on length and time scales that have no influence on the chamber flow – that for purposes of calculating the chamber flow the efflux from the propellant can be treated as locally homogeneous in both space and time. In due course we shall see that this is not the case.

An additional assumption that is made is that the efflux random field (as seen by the chamber flow) can be modelled as a covariance stationary normal process. This simplifies the task of determining the joint probability density function of the process by expressing it as a function of the mean of the marginal distributions and the covariance matrix. This is an issue that is discussed later.

The fluctuations are described in surfaces that are nominally parallel to the propellant surface, and these surfaces are as follows. The physical coordinate system,

tied to the propellant interior, is (ξ, η, ζ) , and the computational coordinate system, tied to the propellant surface, is (x, y, z) . The surface is represented by a single-valued function† via the formula $\eta = f(\xi, \zeta)$ and the relationship between the two coordinate systems is via the formulae

$$\left. \begin{aligned} \xi &= x, \\ \zeta &= z, \\ y &= \eta - \max[f(x, z)] - \gamma(y)\{f(x, z) - \max[f(x, z)]\}, \end{aligned} \right\} \quad (6)$$

where $\gamma(y)$ is a continuously differentiable function that is 1 for $y=0$, 0 for $y \geq 0.5$ mm. Therefore, $y=0$ defines the propellant surface, and the computational surfaces $y=C|C \geq 0.5$ mm are planes for which the distance from the most elevated point of the surface is C . Our particular choice for γ is

$$\left. \begin{aligned} \gamma &= 1 - 3(y/y_0)^2 + 2(y/y_0)^3, & y \leq y_0, \\ \gamma &= 0, & y > y_0, \\ y_0 &= 0.5 \text{ mm.} \end{aligned} \right\} \quad (7)$$

Note that y defined here is slightly different from the earlier definition in § 2.

The natural time scale for the solid physics is much longer than that for the gas physics, and we are only concerned with a quasi-steady gas phase for which temporal changes only occur because of temporal changes at the propellant surface. We pick a single instance of time and describe the flow field at different distances from the surface. The fluctuations that are seen at any plane originate at the surface but evolve with distance from the surface because of mixing and chemical reaction. At the surface there are fluctuations in temperature, mass flux, and reactant concentration. The first two are intimately related via the pyrolysis laws, but even if the surface temperature were uniform the mass flux would not be, because of the heterogeneity of the surface. The gas-phase reactions are affected by the surface temperature (the supply temperature of the reactants), and by the reactant fluxes, and the spatially non-uniform heat released by the reactions has a large affect on the gas temperature, the density, and the velocity field.

The chemical heat release, conducted against the flow to the surface, also strongly affects the surface temperature, and a large portion of the heat flux to the surface is generated by the leading edge of the diffusion flame supported by the mixing of oxidizer flow and binder flow. Because of this, regions on the surface close to a fuel–oxidizer interface have larger surface temperatures than elsewhere. Consequently, it is in these regions that the mass flux leaving the surface is greatest, as demonstrated in figure 7. The four panels of figure 7 show the normal velocity, the temperature, the oxidizer/fuel composition and the corrugation at the surface of P82_390 at a single time. Looking at the velocity panel, the regions of bright red are located at the interface between oxidizer and binder, the yellow-green regions are located on the oxidizer particles, which support the monopropellant decomposition flame, and the dark blue regions are located on pure binder which does not support a flame.

4.1. Edge of the combustion layer

The length scale of the velocity fluctuations shown in figure 7 appears to be directly defined by the scale of the oxidizer particles. It is clearly of interest to examine

† For aluminized propellants, not discussed here, such a representation is not possible and a level-set strategy must be adopted, see Wang & Jackson (2005), Wang *et al.* (2007a).

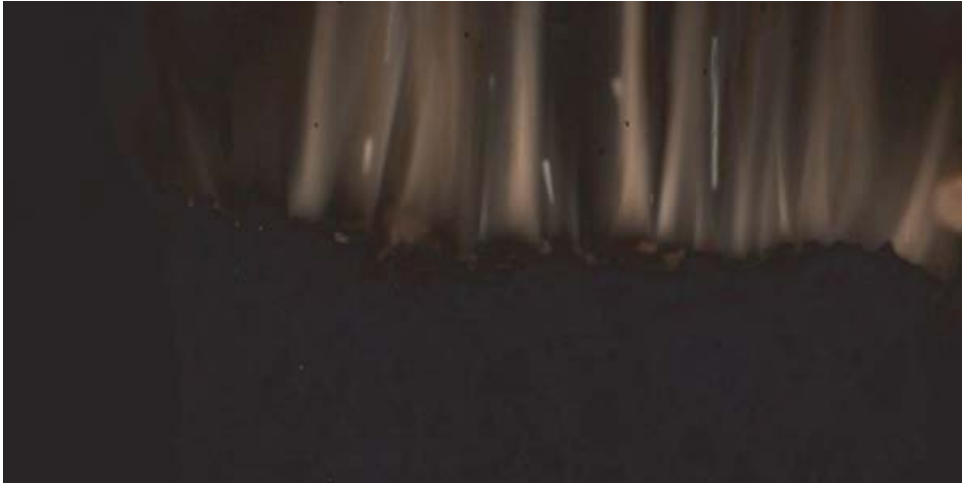


FIGURE 6. Jet like structures photographed above a burning propellant, courtesy Alice Atwood, China Lake.

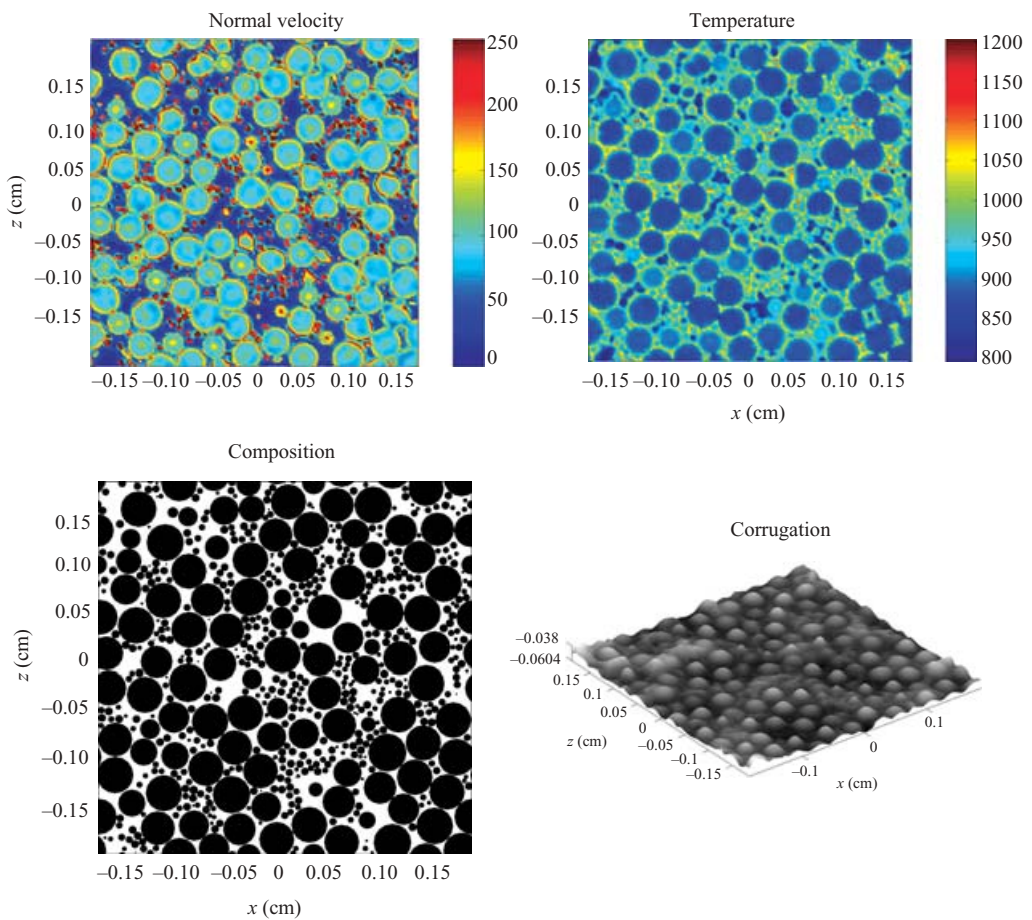


FIGURE 7. Surface properties for P82.390 burning at 20 atm. Velocity in cm s^{-1} , temperature in Kelvin.

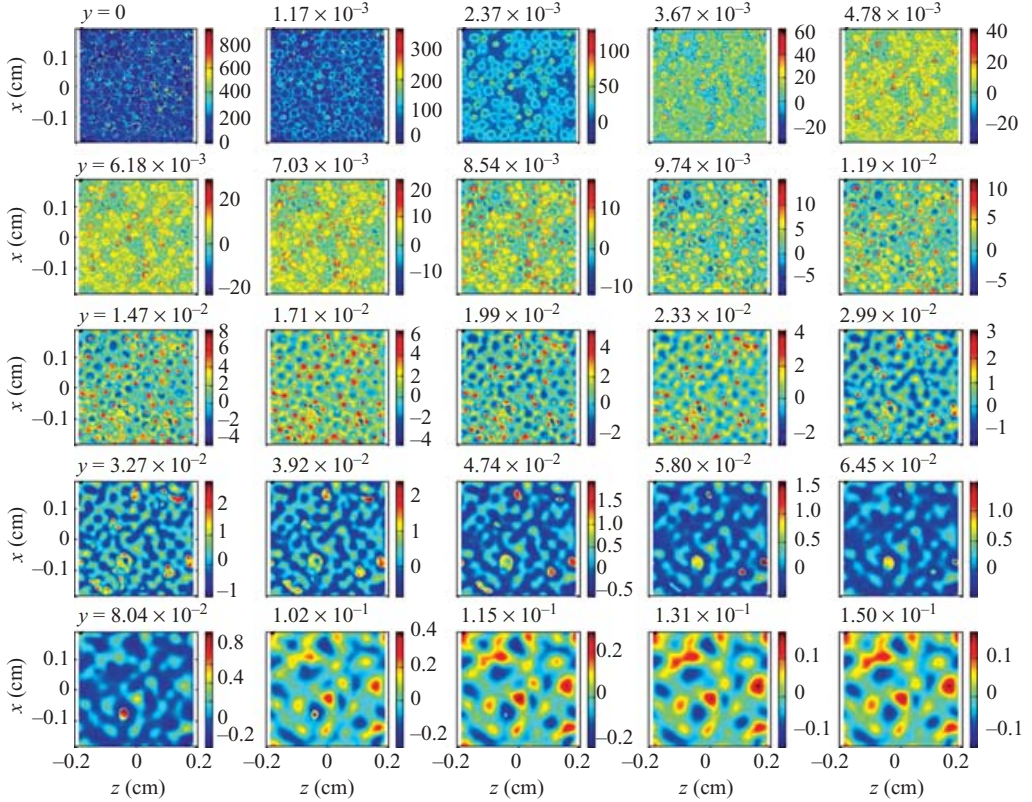


FIGURE 8. Velocity divergence (m s^{-1}) for the P82_390 pack for different values of y (cm).

how this changes as one moves away from the surface, particularly to the region intermediate between the combustion field and the chamber flow field.

The outer edge of the combustion field can be identified as where the chemical-kinetics terms are no longer important to the development of the fluctuations. When all the chemical reactions are exhausted, the perturbations are merely convected and damped by the diffusive flow, physics governed by the Navier–Stokes equations for a non-reacting mixture. Kinetics terms affect the mechanical part of the equations by modifying the continuity equation, so that the divergence of the velocity is large and positive. For the bimodal pack P82_390 in table 1, this divergence is shown in figure 8. Each of the following pairs of numbers lists y in microns followed by representative values of the divergence: (0,100), (48, 10), (119, 3), (299, +1 to –1), (645, +0.2 to –0.2), (1500, +0.1 to –0.1). Note that there are small patches of negative divergence for $y = 119 \mu\text{m}$, and significant regions for $y = 299 \mu\text{m}$ so that, roughly speaking, chemistry is unimportant in this sense beyond $200 \mu\text{m}$. In the following discussion we shall choose $y = 500 \mu\text{m}$ as the plane representative of the intermediate region: half a millimetre is firmly outside the combustion field, but shy of the chamber flow because of the latter’s large scale.

The spatial evolution of the velocity fluctuations is illustrated in figure 9, which shows a number of horizontal slices through the flow field. It is apparent that at 1.5 mm from the surface there are four jets of flow with maximum speeds in the neighbourhood of 450 cm s^{-1} . These four structures are apparent at $299 \mu\text{m}$, but have

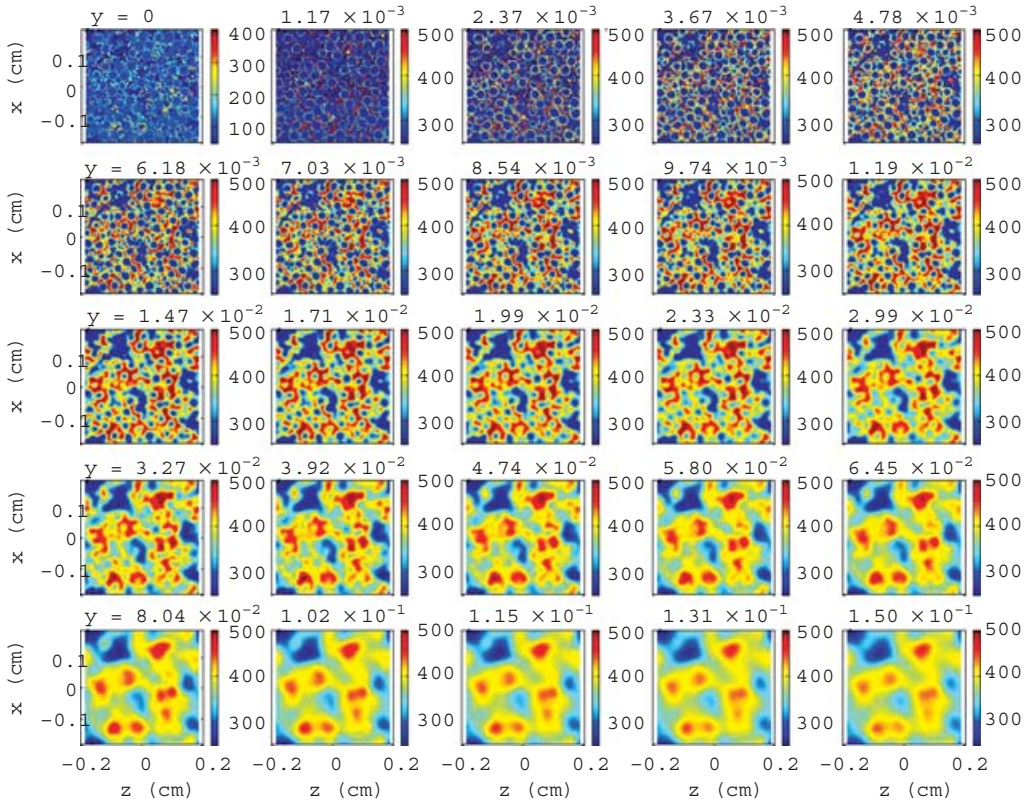


FIGURE 9. Normal velocity (cm s^{-1}) on x, z slices for the P82_390 pack for different values of y (cm).

been significantly smoothed out at the larger distance. It is useful to examine the slower portions of the flow field (blue) rather than the faster portions, because then the pattern clearly visible at 1.5 mm is apparent at 61.8 μm . Moreover, turning back to the first panel of figure 7, its genesis can be seen in the surface distribution. In other words the width of the jets, 1.5 mm or so, has its roots in the clustering of the oxidizer particles at the surface.

Figure 10 shows the temperature fluctuations. There are four hot spots at large values of y , roughly matching the four velocity jets, but here also the pattern is best seen by looking at the low values, the five blue regions. This pattern also can be seen close to the surface, not because the far-field temperature is controlled by the surface temperature, but because it is controlled by the reactant fluxes, and these are linked to the surface velocity.

It is noteworthy in both figure 9 and figure 10 how non-uniform the fields are, how much they differ from a one-dimensional description of the kind that would be generated by a QSHOD (quasi-steady, homogeneous, one-dimensional) strategy (Brewster 2000). Thus at $y = 0.474$ mm the mean velocity is 375 cm s^{-1} , the standard deviation is 56 cm s^{-1} , and the difference between the minimum and maximum velocities is 370 cm s^{-1} . For the temperature, the mean is 2770 K, the standard deviation is 158 K, and the difference between the minimum and maximum values is 772 K. These variations have not been calculated before.

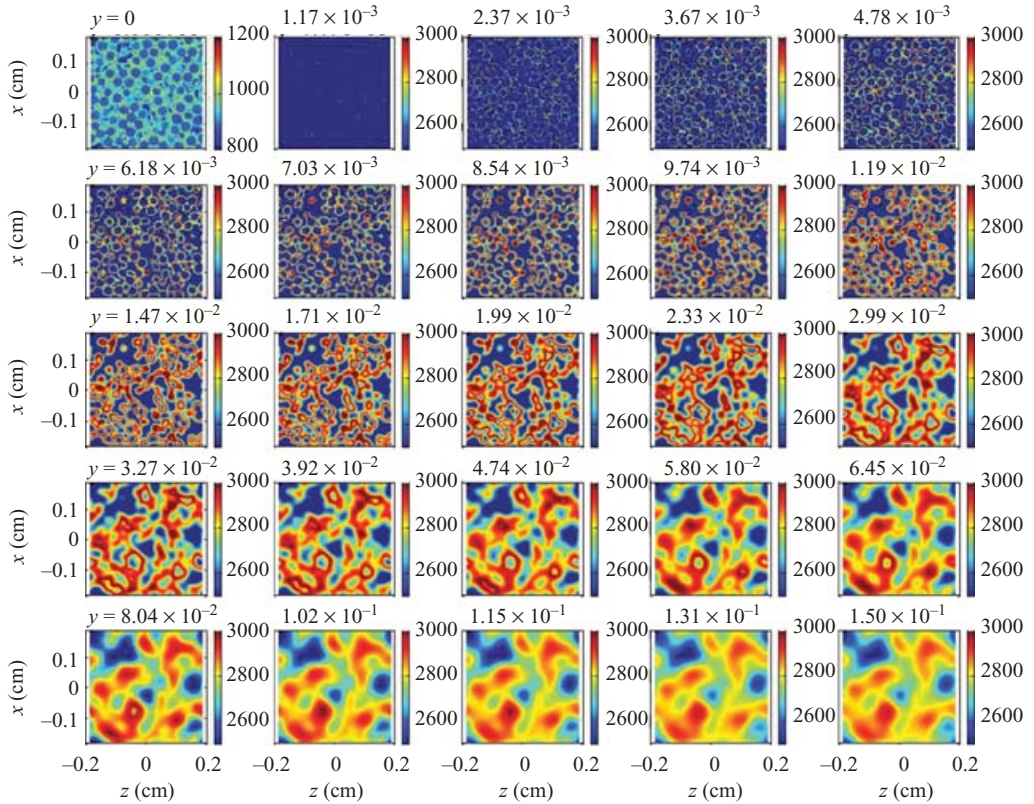


FIGURE 10. Temperature (K) on x, z slices for the P82_390 pack for different values of y (cm).

Figure 11 and figure 12 show vertical cuts through the combustion field, and include part of the propellant pack. These figures show the merging of the hot fast-moving regions as the distance from the surface increases.

5. Fluctuation statistics

In the previous section we gained some insight into the nature of the fluctuations above the propellant surface, particularly in the intermediate region at the edge of the combustion layer. These originate in the heterogeneity of the propellant, and not through any influence of fluctuations in the chamber flow on the combustion field; as noted in §4 we describe the nature of the perturbations generated by the heterogeneity and their impact on fluctuations in the chamber flow, but not the reverse.

The efflux from the burning surface is a random vector field with four components: the normal velocity (v), the temperature (T), and the two tangential velocity components. This field is statistically homogeneous in the x - and z -directions, but not in the y - (normal) direction, and so the marginal probability density functions (p.d.f.s) depend only on y . These functions are plotted for several values of y in figure 13, figure 14, and figure 15. The tangential velocities are small at around 0.5 mm, and so are neglected in the chamber flow analysis discussed in §6; henceforth, we shall only discuss v and T . Then the description of the stochastic process is based upon the definition of a vector Y containing the time-space sequence of the inflow random variables $\{v_n^m, T_n^m\}$ evaluated at time steps $n = 1, \dots, N$, and all the coherently correlated spatial locations

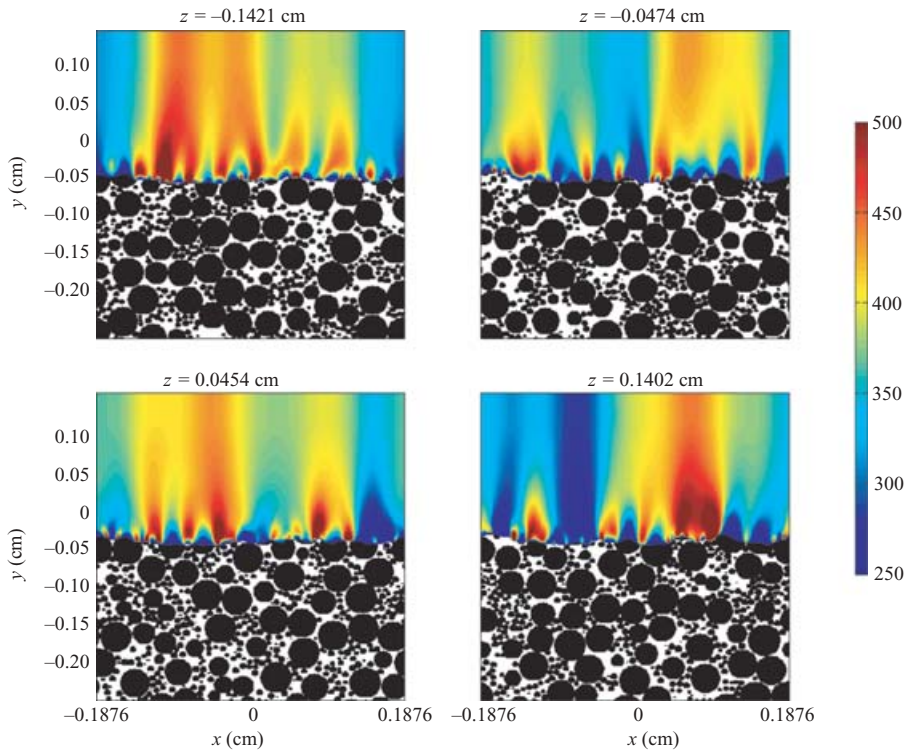


FIGURE 11. Normal velocity (cm s^{-1}) on vertical slices for the P82_390 pack for four values of z (cm).

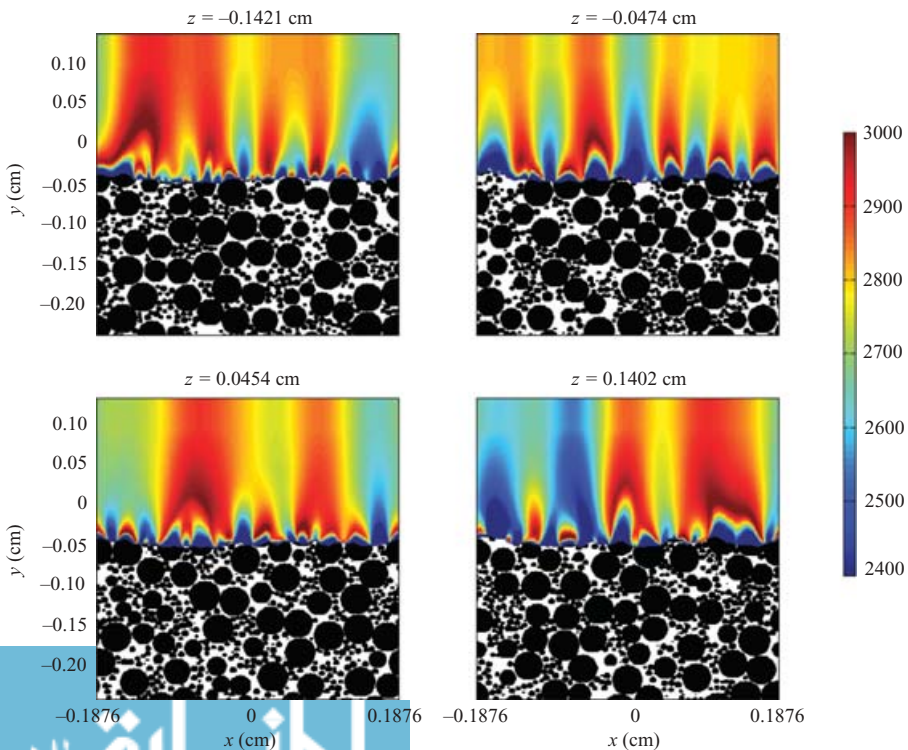


FIGURE 12. Temperature (K) on vertical slices for the P82_390 pack for four values of z (cm).

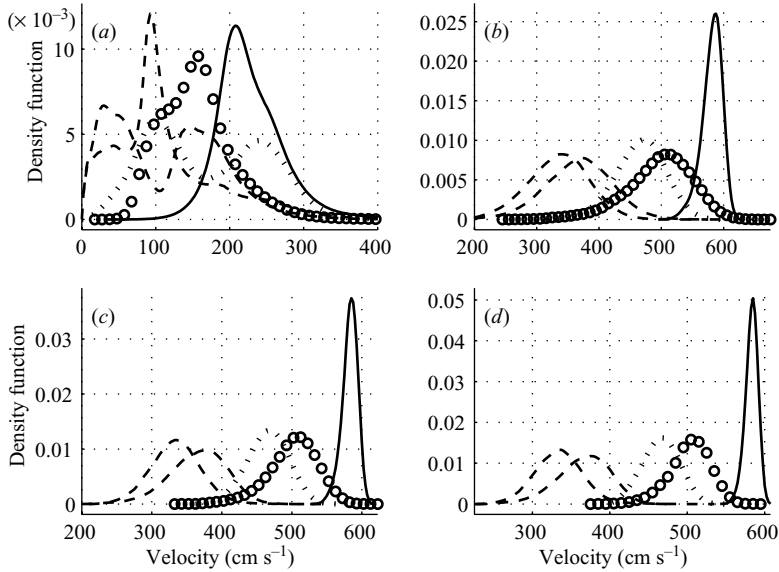


FIGURE 13. Probability density function for the normal velocity at four values of y : dotted line, Th20_50_200; dashed line, H200; solid line, P82; dash/dot line, P82_390; circles, Th200. (a) $y = 0$, (b) $y = 0.05237$ cm, (c) $y = 0.1019$ cm, (d) $y = 0.15$ cm.

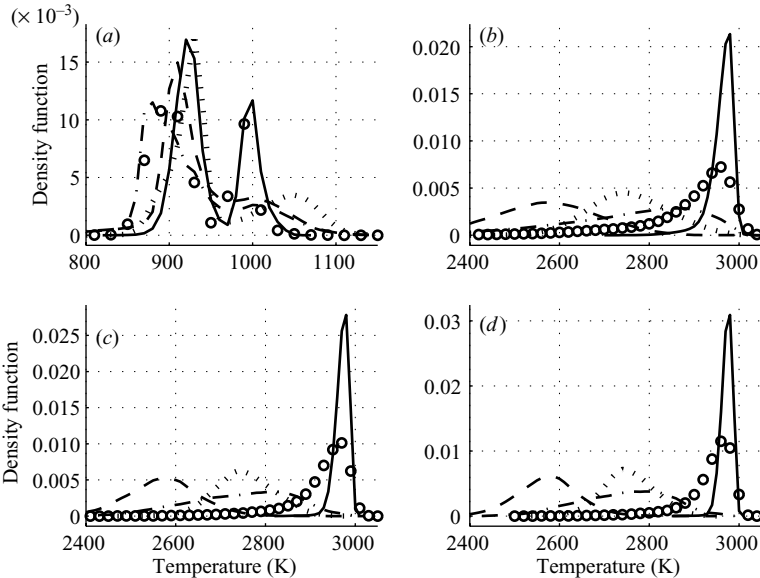


FIGURE 14. Probability density function for the temperature at four values of y : dotted line = Th20_50_200; dashed line = H200; solid line = P82; dash/dot line = P82_390; circles = Th200. (a) $y = 0$, (b) $y = 0.05237$ cm, (c) $y = 0.1019$ cm, (d) $y = 0.15$ cm.

$m = 1, \dots, M$. The associated covariance matrix is

$$K := E[(Y - E[Y])(Y - E[Y])^T], \quad (8)$$

where $E[\cdot]$ represents the expected value or mean, and the superscript T indicates the matrix transpose.

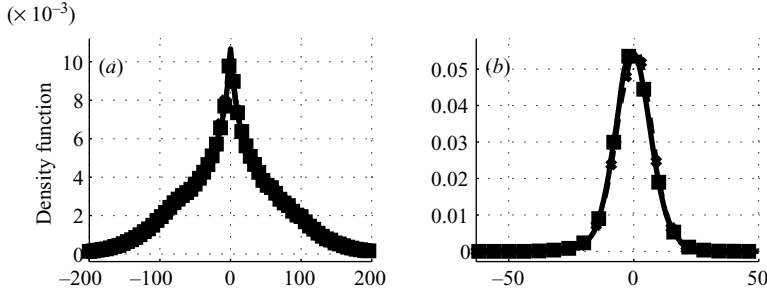


FIGURE 15. Probability density function for the tangential velocity components at two values of y for P82_390. Dashed line with \times marks: U component; solid line with square marks: W component. (a) $y=0$, (b) $y=0.05237$ cm.

Variable	Th20_50_200	H200	P82	P82_390	Th200
Velocity μ	4.66	3.35	5.81	3.67	4.97
Velocity σ	0.40	0.48	0.17	0.54	0.53
Velocity ζ	6.8×10^{-2}	5.1×10^{-2}	1.9×10^{-1}	5.2×10^{-2}	1.7×10^{-1}
Velocity τ	-0.2586	-0.0583	-0.6930	-0.1203	-0.6186
Temperature μ	2755	2572	2962	2756	2888
Temperature σ	89	113	27	152	109
Temperature ζ	5×10^{-2}	3.8×10^{-2}	4.3×10^{-1}	2.8×10^{-1}	5.7×10^{-1}
Temperature τ	0.0480	0.055	-2.0936	-0.6836	-1.8257

TABLE 2. Mean, μ , standard deviation, σ , deviation from a normal distribution, ζ , and scaled third-order moment, τ , for temperature and normal velocity. The temperature is in K, the velocity in m s^{-1} .

Returning to figures 13 and 14, the p.d.f.s. change significantly from the surface, panel (a), to the location at 0.5 mm, panel (b). Variations above 0.5 mm are caused by diffusion, and this damps out the fluctuating part. The change between the fluctuation statistics at the surface and at 0.5 mm is large compared with the change over the interval [0.5, 1.5] mm. This observation supports the idea that thermal expansion and chemical reactions are important in defining the statistics of the fluctuations at the edge of the combustion sublayer.

The p.d.f.s are, approximately, normally distributed for values of y greater than 0.5 mm. Values for the first and second fluctuation moments about the mean for the 0.5 mm planar cut are listed in table 2. There, ζ is a parameter that quantifies the difference between a p.d.f. $\Gamma(x)$ and the approximating normal density function with equal first and second moments:

$$\zeta = \int_{-\infty}^{+\infty} dx \left| \Gamma(x) - \frac{\exp\left(-\frac{1}{2}\left(\frac{x-\mu}{\sigma}\right)^2\right)}{\sigma\sqrt{2\pi}} \right|. \quad (9)$$

In addition, the variable $\tau = \mu^{III}/\sigma^3$ in table 2 quantifies the skewness of the distribution where μ^{III} is the third-order moment about the mean; for a symmetric distribution, $\tau = 0$.

In general we note that the hypothesis of normal density is satisfied for the velocity better than for the temperature. For the velocity, the two packs with multi-modal distributions (P82_390, Th20_50_200) yield marginal densities that are the closest to normal distributions. P82_390 yields the smallest τ . For the temperature, Th20_50_200

yields a distribution which is the closest to normal. Two packs have temperature p.d.f.s that are significantly different from normal distributions, namely P82 and Th200; they yield a high degree of skewness.

These observations, and the fact that industrial propellants are most often poly-dispersed (and so P82 and Th200 are not representative), lead us to the choice/assumption that the fluctuations constitute a covariance stationary normal process, one in which the covariance kernel is a function of time-space differences only, and the distribution is multi-normal. The task of determining the joint probability function of the process is thereby facilitated, since it is then completely determined from knowledge of the process covariance matrix and the marginal distributions means. The basic assumptions are:

- (i) any linear combination of the random variables is normally distributed;
- (ii) the covariance kernel K (equation (8)) is stationary in space and time.

Obviously each random variable is normally distributed; and the joint density of the process is

$$g(y) = \frac{\exp\left(-\frac{1}{2}(y - \mu)^\top K^{-1}(y - \mu)\right)}{(2\pi)^{n_p/2} \sqrt{|K|}} \quad (10)$$

where $\mu \in R^{n_p}$ is the vector of the means. We remark that a normal distribution for the marginal densities is a necessary but not sufficient condition for a random vector field to form a normal process, i.e. for the joint probability function to be multi-normal.

5.1. Spatial scales

The spatial scales of the fluctuations can be determined from the autocorrelation coefficient. The autocorrelation for a continuous variable $U(x, t)$ of a random field statistically homogeneous over the domain \mathcal{D} and the time interval \mathcal{T} is evaluated as

$$\rho(h, k) = \frac{\int_{\mathcal{T}} \int_{\mathcal{D}} u(x, t) u(x - h, t - k) dx dt}{\int_{\mathcal{T}} \int_{\mathcal{D}} dx dt}. \quad (11)$$

Here, u is the fluctuation $U - \int_{\mathcal{T}} \int_{\mathcal{D}} U dx dt / \int_{\mathcal{T}} \int_{\mathcal{D}} dx dt$ defined on an x, z planar cut. Note that h is a vector; and the function U is periodic in the box \mathcal{D} , truncated outside \mathcal{T} . The autocorrelation coefficient is $\tilde{\rho} = \rho/\rho(0, 0)$, the spatial autocorrelation is $\rho(h, 0)$, $h \in \mathcal{D}$, and the time autocorrelation is $\rho(0, k)$, $k \in (-\mathcal{T}, \mathcal{T})$.

The spatial autocorrelation coefficients for the normal velocity and temperature are shown in figures 16 and 17. Close to the surface the coefficients drop sharply, indicating that the fluctuations are only correlated over very small scales; they become better organized as the distance from the surface increases. Above $y = 0.5$ mm the coefficients do not change a great deal, and above 1 mm they change minimally.

A characteristic dimension of the random field can be deduced from the curvature of each autocorrelation function at the origin, analagous to the so-called microscale (Tennekes & Lumley 1972). The velocity fluctuation microscale Λ_v , for the five morphologies, is shown in table 3 as a function of the normal distance y ; it changes between the surface and the plane $y = 0.5$ mm by one order of magnitude. When the spatial scale of the fluctuations a millimetre or so from the surface is compared to the scale of the chamber geometries we shall consider, table 4, it is evident that they differ by 3 orders of magnitude. And an examination of the average grid spacing in the streamwise direction, also shown in table 4, suggests that the

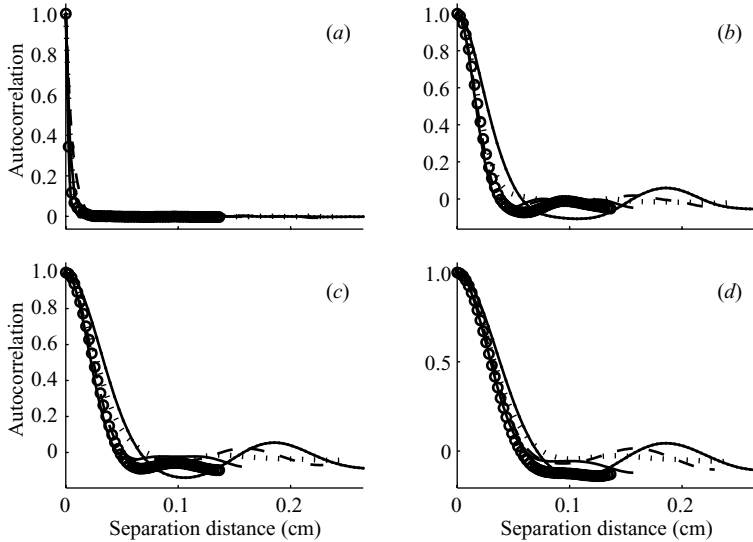


FIGURE 16. Velocity autocorrelation coefficient as a function of the separation distance for the five packs; the distance from the burning surface is: (a) $y=0$, (b) $y=0.05237$ cm, (c) $y=0.1019$ cm, (d) $y=0.15$ cm. Dotted line, Th20_50_200; dashed line, H200; solid line, P82; line with dots, P82_390; circles = Th200.

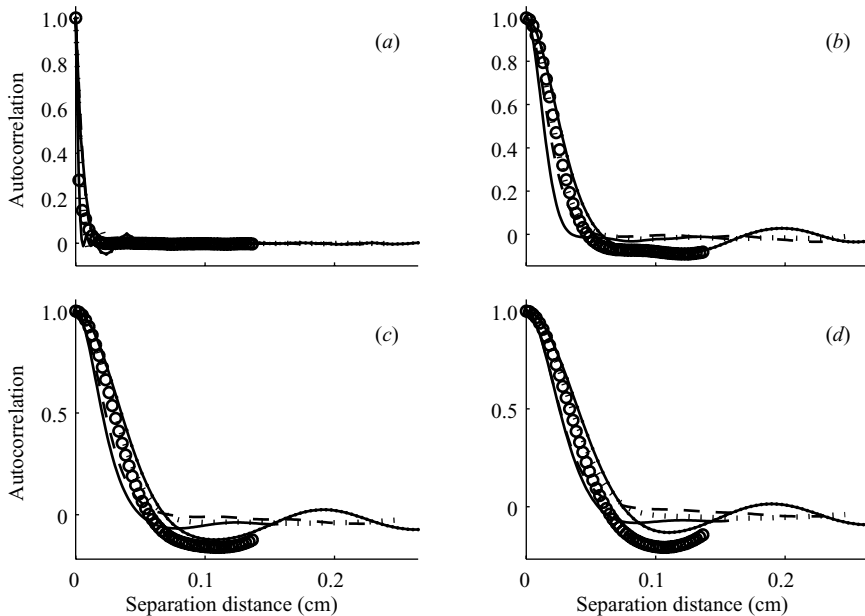


FIGURE 17. Temperature autocorrelation coefficient as a function of the separation distance for the five packs; the distance from the burning surface is: (a) $y=0$, (b) $y=0.05237$ cm, (c) $y=0.1019$ cm, (d) $y=0.15$ cm. Dotted line, Th20_50_200; dashed line, H200; solid line, P82; line with dots, P82_390; circles, Th200.

efflux variables evaluated at neighbouring mesh points are only weakly correlated, and the fluctuations at distinct grid points can be treated as independent stochastic processes.

Pack	$y = 0$	$y = 5 \times 10^{-2}$	$y = 1 \times 10^{-1}$	$y = 1.5 \times 10^{-1}$
H200	2.8×10^{-3}	4.1×10^{-2}	6.1×10^{-2}	7.1×10^{-2}
Th200	3.2×10^{-3}	3.0×10^{-2}	4.2×10^{-2}	5.3×10^{-2}
P82	1.8×10^{-3}	3.1×10^{-2}	4.3×10^{-2}	6.1×10^{-2}
P82_390	2.7×10^{-3}	4.1×10^{-2}	5.9×10^{-2}	7.3×10^{-2}
Th20_50_200	1.7×10^{-3}	3.2×10^{-2}	4.55×10^{-2}	5.5×10^{-2}

TABLE 3. Spatial microscale (cm) based on the fluctuation, Λ_V , for different values of y (cm).

Case	L (m)	L_p/L	H/L	T/H	Δx (m)	\dot{m} (kg m ⁻² s ⁻¹)	T_{inj} (K)
Onera86	0.51	0.94	3.9×10^{-2}	1	1.2×10^{-3}	13.0	260.0
OneraC1	0.47	0.42	1.3×10^{-1}	0.56	3.3×10^{-3}	21.2	3387.0

TABLE 4. Summary of the chamber geometries considered. Both test cases assume two-dimensional planar flow. L is the total length of the chamber, L_p is the length of the propellant section, H is the height, T is the minimum height, Δx is the streamwise grid spacing at the surface, averaged over the propellant section; refer to figure 21 for a better explanation of the geometry. \dot{m} and T_{inj} are the average mass flux and temperature over the propellant section.

It does not follow, of course, that just because the correlation length is much smaller than the mesh size these correlations have no effect on the turbulence field in the chamber. Rather, these disparate numbers reveal a challenging issue in the study of turbulence in injected flows. For the model rocket configurations that we shall consider, the Kolmogorov scale is typically 10 μm , and so eddies of size 10–1000 μm are subgrid. Large-eddy simulations (LES) can successfully account for the contribution that these make to the field equations, but strategies to account for fluctuations at the injection boundaries are not well established. Past rocket-flow simulations use LES with white-noise fluctuations at these boundaries, thus uncorrelated both in space and time, e.g. Wasisto & Moser (2005). The grid resolution study and comparisons with DNS results and experimental data reported in Wasisto *et al.* (2004) provide strong evidence that converged solutions can be obtained in this situation using LES. But we cannot be sure that the subgrid forcing that we have identified does not lead to an energy flow to larger scales, either because a significant component of the disturbance ‘shape’ corresponds to eigenfunctions of unstable modes, or through unknown nonlinear processes. This leaves us with two choices: to terminate our discussion until such time as a strategy is developed for accurately including any contribution that these disturbances might make; or to continue, to see if, when time correlations are examined, results different from those generated by white noise are obtained. We shall continue.

5.2. Time correlations and scales

In examining time correlations we focus on the $y = 0.5$ mm plane, because we choose this as the boundary between the chamber and the propellant subdomains. Velocity and temperature autocorrelations and the velocity–temperature correlation coefficient are shown in figure 18. This information, multiplied by the standard deviations of table 2, is fed into the normal process. The pack morphology has a strong effect on the time correlations, stronger than on the spatial correlations, and large-sphere packs such as Th200 yield a wider correlation curve than small-sphere ones such as P82. However, it is not just the largest dimension that is important in determining

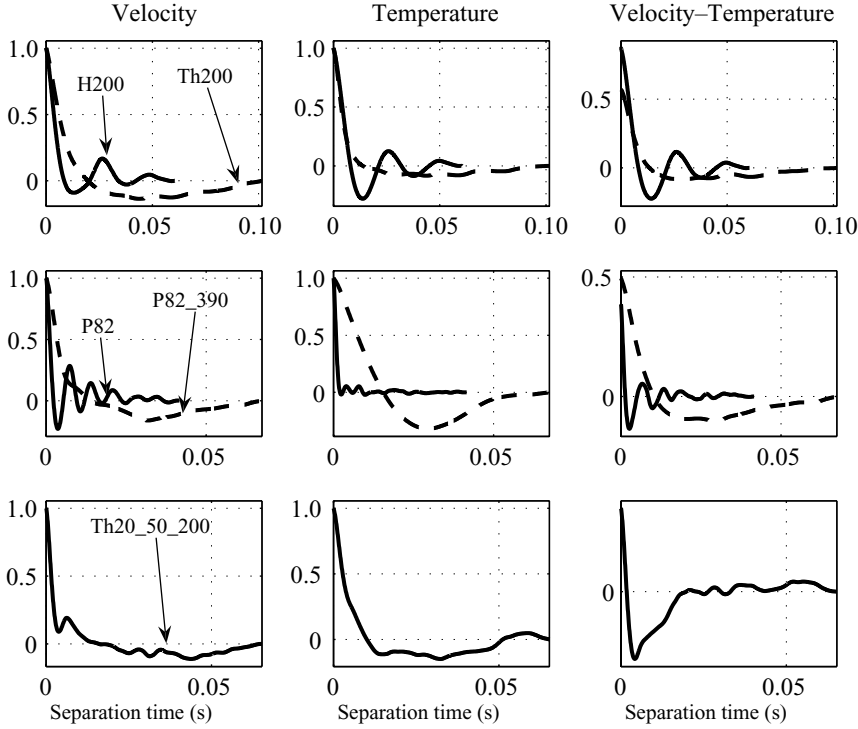


FIGURE 18. Time correlations for the five morphologies; pack morphologies are the same across the rows.

the shape of the curve, but also the overall distribution. Consider, for example, results for the Th20_50_200 morphology, figure 18 (g). The curve comprises two segments, the first typical of small-sphere packs, the second typical of large-sphere packs. This behaviour can be explained by analysing the spectral densities and considering the link between spectral density and time autocorrelation. We define scaled spectral densities of the velocity and temperature fluctuations as

$$\delta_{\{v,T\}}(\kappa) = \frac{\mathcal{F}[\{v,T\}](\kappa)\mathcal{F}^*[\{v,T\}](\kappa)}{\rho(0,0)} \quad (12)$$

where \mathcal{F} indicates the Fourier transform of the fluctuation u of a random variable U for the truncated process of length \mathcal{T} ,

$$\mathcal{F}[U](\kappa) = \frac{1}{\mathcal{T}} \int_{t_0}^{t_0+\mathcal{T}} \exp(-i2\pi\kappa z)u(z) dz. \quad (13)$$

The spectral densities for the two state variables are shown in figure 19. The correlation coefficient of figure 17 can easily be related to the spectral density:

$$\tilde{\rho}_{\{v,T\}}(0,k) = 2\mathcal{T} \int_0^\infty \delta_{\{v,T\}}(\kappa) \cos(2\pi\kappa h) d\kappa. \quad (14)$$

Note that this equation remains an identity in the discrete sense when the spectral density is defined using the discrete Fourier transform and a discrete sample average is used to evaluate the autocorrelation. The particular shape of the velocity autocorrelation function for Th20_50_200 is due to the large values associated with high-frequency modes in the spectral density curve. These are indicative of a high

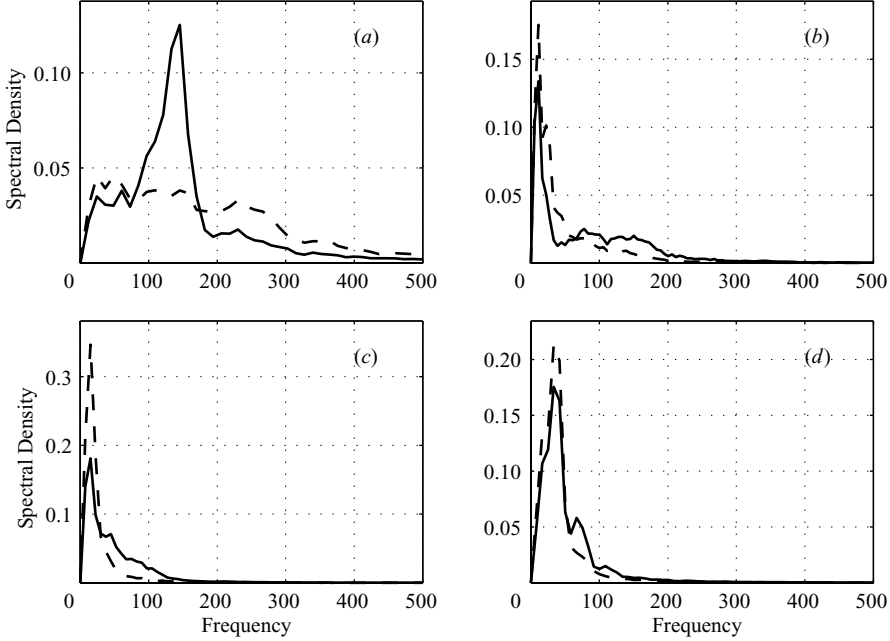


FIGURE 19. Velocity and temperature spectral densities. Solid line: velocity fluctuation; dashed line; temperature fluctuation. (a) P82, (b) Th20_50_200, (c) P82_390, (d) H200.

percentage of fine AP. When the large-frequency modes are weak, as in P82_390 for which the fraction of fine AP is small, the autocorrelation curve is less steep.

The temperature autocorrelation curve for Th20_50_200 does not seem to be affected by the presence of small oxidizer particles. Indeed, the fine AP cut appears to be of little significance for the temperature fluctuation statistics of all packs, and this is reflected by the temperature spectral density curves. Compare this with the velocity spectral density curve for P82, for example, which displays a well-defined maximum. Clearly, the velocity and temperature fluctuations are due, in part, to different phenomena.

The fluctuations define a time scale, just as they define a length scale. This can be determined from a quadratic approximation of the autocorrelation near the origin:

$$\tilde{\rho}_{\{v,T\}}(0, k) = 1 - k^2/\lambda_{\{v,T\}}^2 + O(k^4). \quad (15)$$

Thus

$$\lambda_{\{v,T\}}^2 = \frac{\int_0^\infty \delta_{\{v,T\}}(\kappa) d\kappa}{2\pi^2 \int_0^\infty \kappa^2 \delta_{\{v,T\}}(\kappa) d\kappa}, \quad (16)$$

and from this we conclude that the large-frequency Fourier components are important in determining λ because of the factor κ^2 in the denominator. The characteristic times of the fluctuations are listed in table 5. Note that the velocity microscale differs significantly from the temperature microscale for packs with high concentrations of fine AP. For these morphologies, high-frequency oscillations contribute to reducing the curvature radius at the origin for the velocity autocorrelation, but not for the temperature.

Pack	λ_V (s)	λ_T (s)	r_b (cm s ⁻¹)	\dot{m} (g cm ⁻² s ⁻¹)	T_f (K)
H200	2.1×10^{-3}	2.5×10^{-3}	0.65	1.08	2572
Th200	2.6×10^{-3}	2.5×10^{-3}	0.81	1.38	2888
P82	1.1×10^{-3}	0.8×10^{-3}	0.97	1.69	2962
P82_390	2.3×10^{-3}	3.3×10^{-3}	0.71	1.11	2756
Th20_50_200	1.4×10^{-3}	2.1×10^{-3}	0.86	1.40	2755

TABLE 5. Temporal microscale based on velocity (λ_V) and temperature (λ_T) fluctuations, regression rates (r_b), average mass flux (\dot{m}), average flame temperature (T_f) for the five packs. Pressure is 20 atm.

5.3. Implementation

Given a vector, X , of identically independently normally distributed variables with zero mean and standard deviation equal to 1, a multinormal distribution with assigned mean μ and covariance matrix K is obtained as

$$Y = H X + \mu, \quad H H^T = K. \quad (17)$$

The advantage of such a formulation is rooted in the fact that the covariance matrix is symmetric positive definite. Therefore matrix factorization can be carried out using a Cholesky decomposition, which yields a lower-triangular H matrix. Obviously, the size of Y increases proportionally to the simulated time, and factoring the matrix at each time step of a fluid simulation is an order n_p^3 operation. A property of the Cholesky factorization is that any row of the triangular matrix is independent of rows with greater index, so that at each time step only the rows associated with the current time variables need to be evaluated, which requires order n_p^2 operations. Nonetheless, in the computations reported below the number of time steps of around 10^{-7} s needed to obtain a statistically accurate description of the flow solution is of the order of 10^7 . It is not possible therefore to retain all of the random variables in the time sequence. When all the correlation coefficients become smaller than some threshold value, we truncate the time sequence, effectively setting $K_{c,d} = K_{d,c} = 0$, where c marks the entry to be computed and d marks the discarded one. In order to maintain continuity of the process, for the truncated sequence we evaluate the components of the Y vector at the current time iteration using a slightly different strategy from that described above. We derive the conditional probability density for the truncated sequence at the current time, Y_c , given the knowledge of the efflux at n_p (only) previous times:

$$\begin{aligned} f_c &:= f_{Y_c|Y_{c-n_p}, Y_{c-n_p+1}, \dots, Y_{c-1}}(y_c|y_{c-n_p}, y_{c-n_p+1}, \dots, y_{c-1}) \\ &= \frac{1}{\sqrt{2\pi\sigma^*}} \exp\left\{-\frac{1}{2}\left(\frac{y_c - \mu^*}{\sigma^*}\right)^2\right\}. \end{aligned} \quad (18)$$

Equation (18) shows that Y_c is normally distributed with mean

$$\mu^* = \mu - \sum_{j=0}^{n-1} \frac{K^{-1}_{j,n}}{K^{-1}_{n,n}} (x_j - \mu_j)$$

and standard deviation

$$\sigma^* = \frac{1}{\sqrt{K^{-1}_{n,n}}}.$$

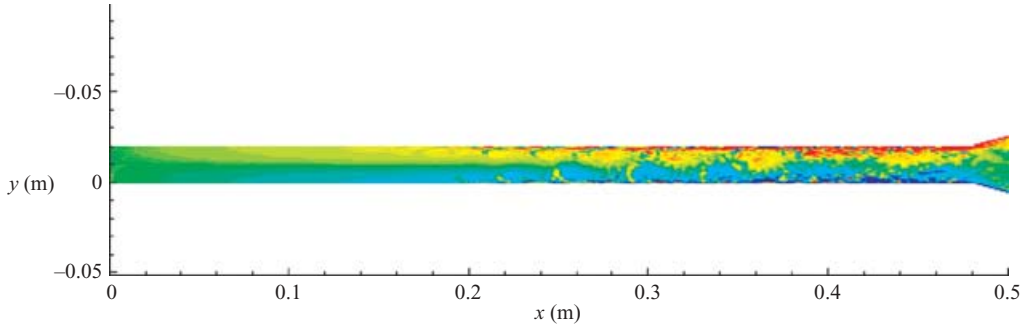


FIGURE 20. Spanwise vorticity colourmap for the Onera86 test case. The vorticity colormap minimum, maximum value and step are $(-5 \times 10^4, 5 \times 10^4, 5 \times 10^3)$ sec^{-1} respectively.

The implementation of the normal process requires only the computation of identically independently normally distributed numbers. The well-known Box–Muller method is used for the generation of normal random variates (Box & Muller 1958).

6. Chamber-flow analysis

The physical domain is divided into two sub-domains. The propellant sub-domain comprises the solid phase and the combustion layer, the region of fluid where chemical reactions are important and the heat flow is large. The chamber sub-domain is where the non-reacting Navier–Stokes equations apply. This division is one of the foundations of our approach, and relies on a subgrid micron-scale model to determine the fluctuations, and a fluid Navier–Stokes solver for a non-reactive mixture to analyse the flow in the chamber. Earlier reports of the chamber-flow code that we use are given in Wasistho & Moser (2005) and Wasistho *et al.* (2004); the latter carefully examines accuracy and convergence questions. Unlike the combustion code, the fluids code is compressible.

Another key ingredient is the assumption, noted earlier, that the fluctuation statistics is dependent only on the propellant morphology and the chamber pressure, for this allows us to describe the fluctuations independently of the chamber flow. As a consequence of the decoupling, the propellant sub-system is simulated with a zero-flux far-field boundary condition for the temperature and a zero-shear far-field boundary condition for the momentum equations. Periodic boundary conditions are applied to the propellant sub-domain in the directions perpendicular to the main regression speed. As a consequence of the randomness of the packing and the absence of boundary forcing, fluctuations measured on planes perpendicular to the mean burning direction constitute a statistically homogeneous random field. The absence of an external time scale makes the random field statistically homogeneous in time as well. Also, because of the decoupling, the space–time-varying inflow in the fluid sub-domain is treated as simple boundary forcing.

Two chamber geometries are considered, test beds used by others with the labels Onera86 and OneraC1. All of our calculations are two-dimensional (planar), and three propellants are examined, P82, Th20_50_200, and P82_390, corresponding to weak forcing, medium forcing, and strong forcing.

Onera86 (Traianeau, Hervat & Kuentzmann 1986), is essentially a straight open-ended tube (see figure 20) and has been widely used to study turbulence modelling in porous wall geometries. The calculations are characterized by cold flow, although there are both velocity and temperature fluctuations at the wall.

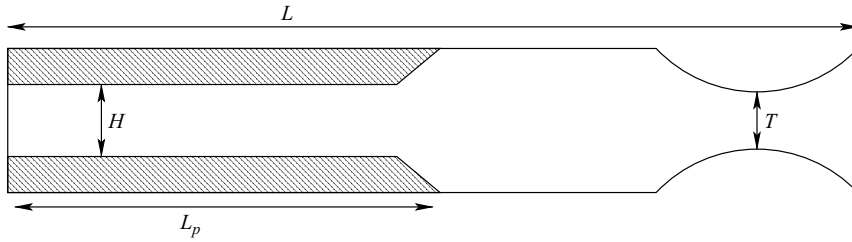


FIGURE 21. Sketch of the chamber geometry used (see table 4). The shaded regions represent the propellant.

OneraC1 has a geometry that more closely resembles an actual rocket chamber, with a Laval nozzle preceded by a streamwise step which gives rise to shear layers and vortex shedding (figure 21). It is a configuration that has been used in numerical simulations at Onera (Lupoglazoff & Vuillot 1992) and here we report hot-flow results. The parameters for both geometries are identified in table 4.

6.1. Scaling the fluctuations

The calculations of the chamber flow require the specification of data at each boundary mesh point. The fluctuation data are independent of those at other mesh points because, as we noted earlier, the spatial correlation lengths are an order of magnitude smaller than the mesh size for the chamber.

At each boundary mesh point, one that corresponds to what we have called an intermediate point, 0.5 mm above the propellant, it is necessary to impose a time sequence of values of v and T where v is the normal velocity and T is the temperature. This time sequence must match the statistics that we have calculated, and these are: the time autocorrelations of v and T ; the time cross-correlations of v and T ; and the joint p.d.f. of v and T . The span of the time sequence is large compared to the correlation times.

The sequence, averaged in time, defines both a mean equilibrium or flame temperature (and so a mean density), and a mean velocity (and so a mean mass flux). These values are different for different propellants (when the mean pressure is fixed), and different from the test-bed values defined in table 4. And so we scale the temperature sequence for each propellant so that the time average of the mass flux is equal to the test-bed value; and we scale the velocity sequence so that the time average of the mass flux is equal to the test-bed value. To convert v to a mass flux requires a value of the mean density, calculated from the equation of state with the local value of pressure and a molecular weight of 34.

6.2. Results for Onera86

The root mean square (r.m.s.) of the velocity fluctuations, which is defined as the standard deviation of pointwise fluctuation time sequences, is plotted against the crosswise coordinate in figures 22 and 23 for different streamwise locations. The effect of the morphology on the chamber flow fluctuations is significant in the streamwise interval $0.150 \text{ m} < x < 0.250 \text{ m}$ where the core-flow normal velocity fluctuations are much larger than the fluctuations at the wall, where the forcing takes place, meaning that considerable growth has occurred. The effect of the forcing is evident in this region where P82_390 yields the largest r.m.s. and P82 the smallest. In the aft region of the rocket the three morphologies yield similar results, and the rms profiles are dependent only upon the geometry and the mean boundary conditions.

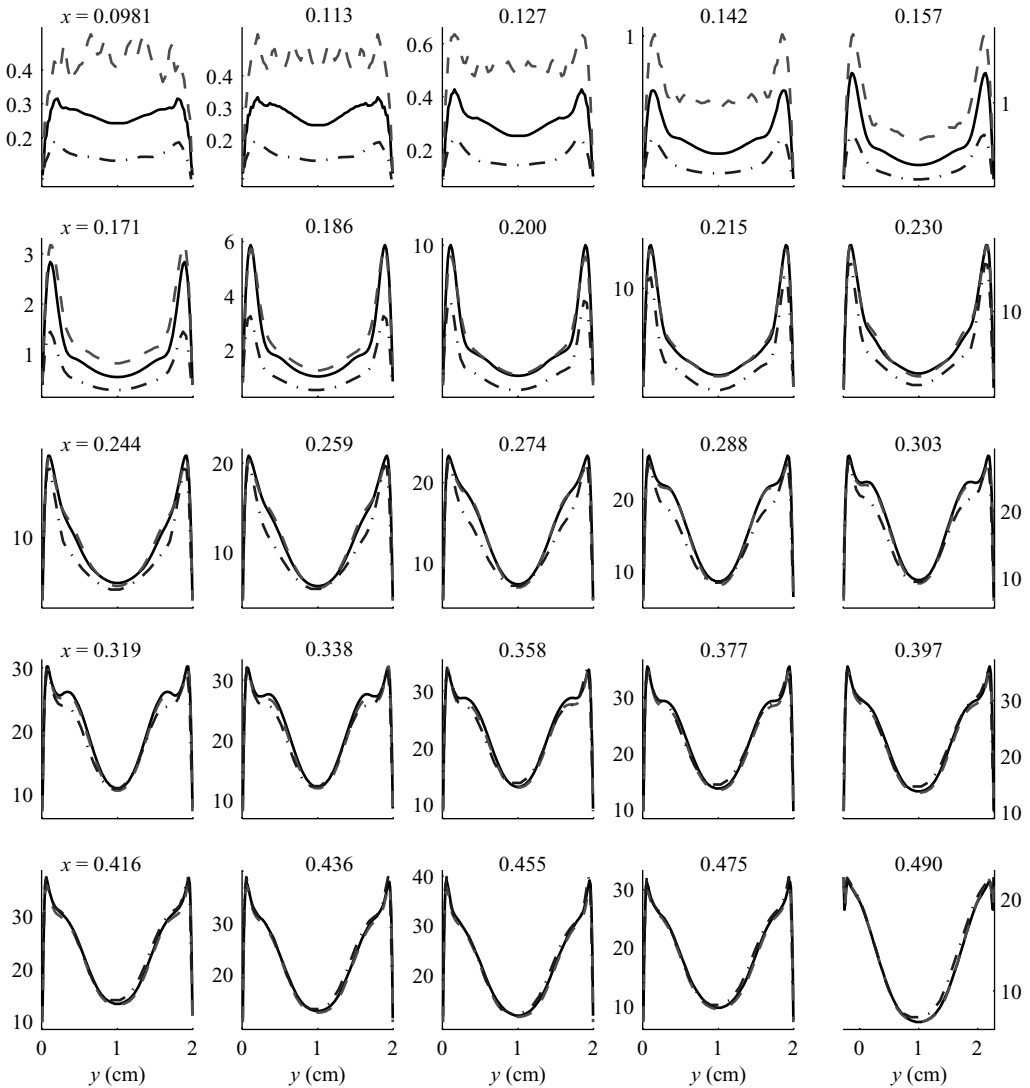


FIGURE 22. Axial velocity component root mean squares for the Onera86 chamber flow, units m s^{-1} : solid line, Th20_50_200; dashed line, P82_390; dash/dot line, P82.

6.3. Results for OneraC1

For this geometry, the vorticity contours at three evenly spaced times are shown in figure 24. The periodic vortex shedding can be clearly seen by comparing panels (a)–(c). We focus on the head-end pressure fluctuations and the shedding frequency.

The head-end pressure oscillation is a design variable whose value is minimized in an optimal design; oscillations with magnitude a few fraction of percent of the mean are considered large. For the OneraC1 case, when morphological fluctuations are not considered, the head-end pressure oscillation is primarily due to vortex shedding. The value of the shedding frequency is close to the second acoustic mode frequency computed in Kouta (1999) as 2750 Hz.

When a real propellant is considered, the forcing associated with the morphology induces head-end pressure fluctuations that are comparable in magnitude to those caused by the periodic vortex shedding. The head-end pressure time traces for the three

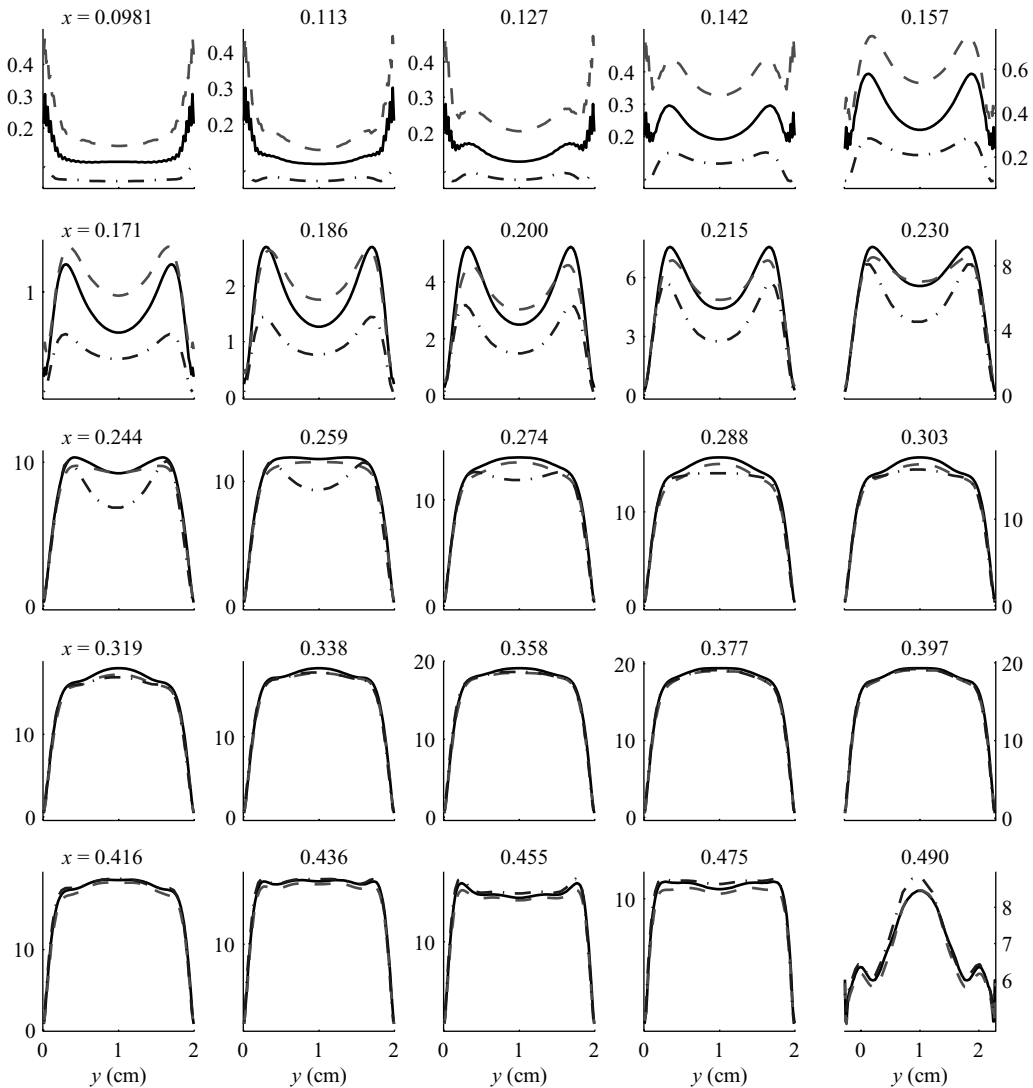


FIGURE 23. Normal velocity component root mean squares for the Onera86 chamber flow, units m s^{-1} : solid line, Th20_50_200; dashed line, P82_390; dash/dot line, P82.

packs and for the non-forced case are shown in figures 25 and 26, on a milliseconds scale and on a seconds scale respectively. The fast oscillation, the one varying with a frequency of the order of 1 ms, is due to the vortex shedding, the slow frequency is due to the morphological forcing. Figure 27 compares the P82_390 results with those obtained using white-noise fluctuations. The head-end pressure oscillation depends strongly on the morphology. The addition of morphological fluctuations causes the standard deviation of pressure oscillations to increase by a factor 1.7, table 6. The strong forcing, P82_390, yields the largest standard deviation.

Figure 28 shows the results of figures 25 and 26 in the frequency domain. This makes it clear that for these small rockets the shedding frequency is not changed by the low-frequency fluctuations at the injection boundary, but the associated amplitude is diminished by morphological scales in the efflux.

In evaluating these results, however, a word of caution. A planar simulation does not consider randomness of the efflux in the spanwise direction, so that fluctuations

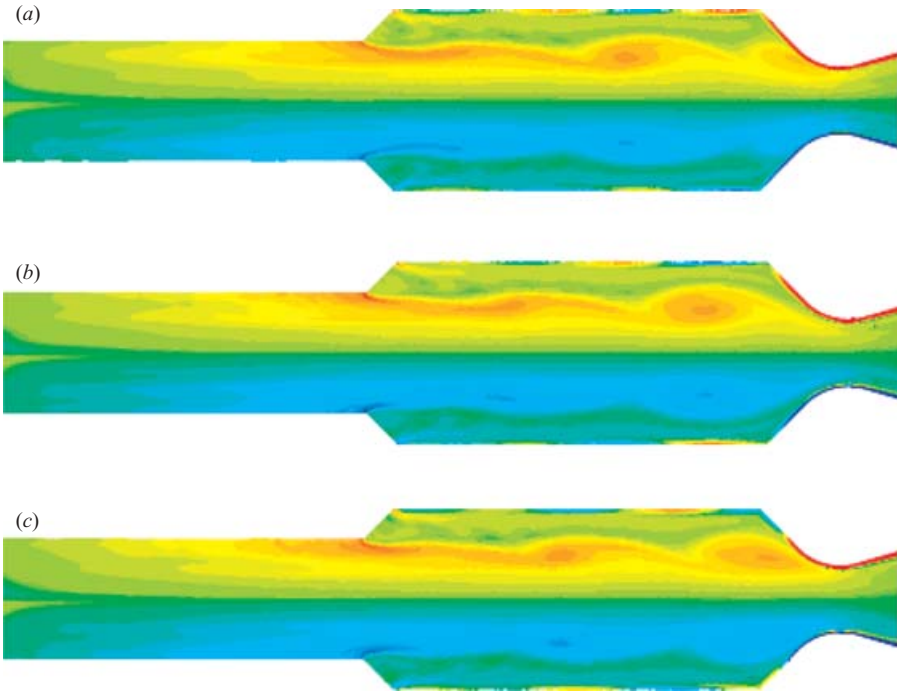


FIGURE 24. Spanwise vorticity colourmap for the OneraC1 test case. Frames (a)–(c) are separated by 1.3×10^{-4} s. Minimum, maximum value and step are $(-5 \times 10^4, 5 \times 10^4, 5 \times 10^3) \text{ s}^{-1}$ respectively.

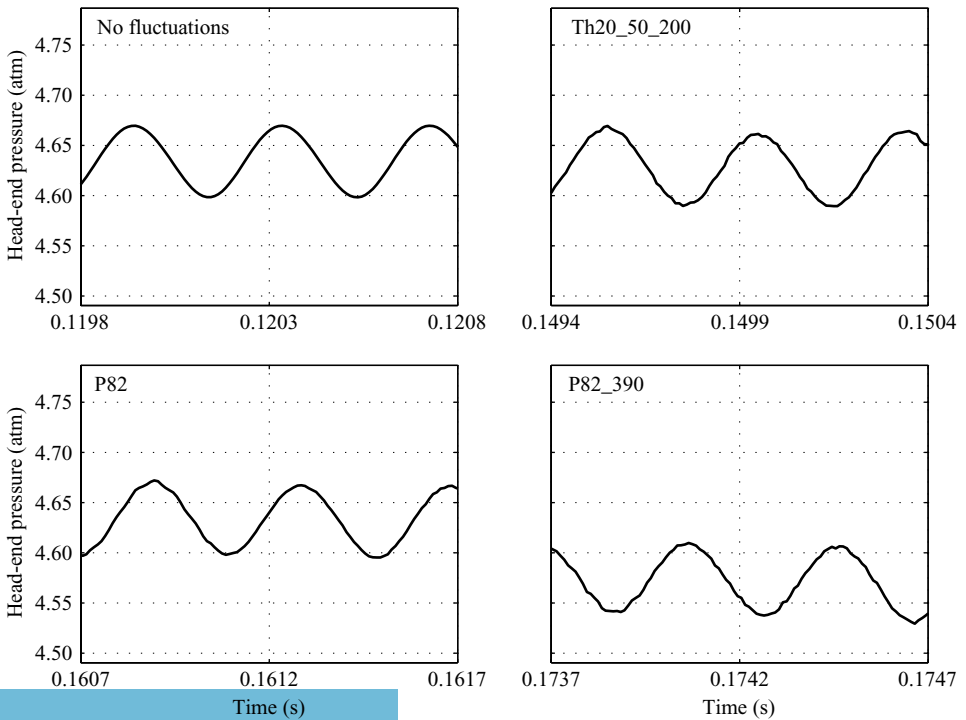


FIGURE 25. Head-end pressure fluctuations for the OneraC1 rocket on a milliseconds scale.

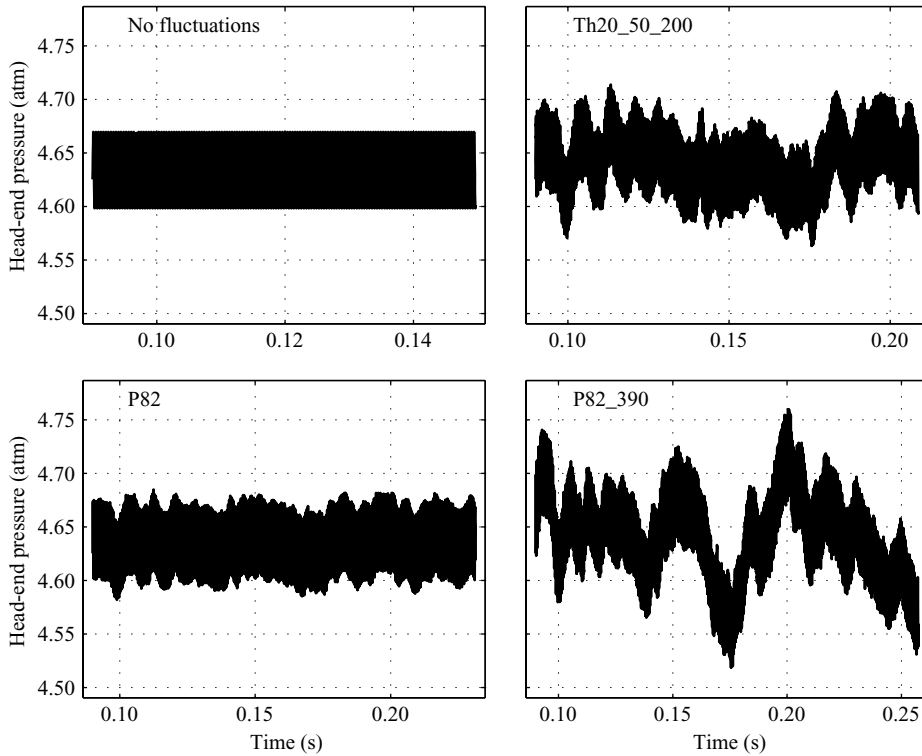


FIGURE 26. Head-end pressure fluctuations for the OneraC1 rocket on a seconds scale.

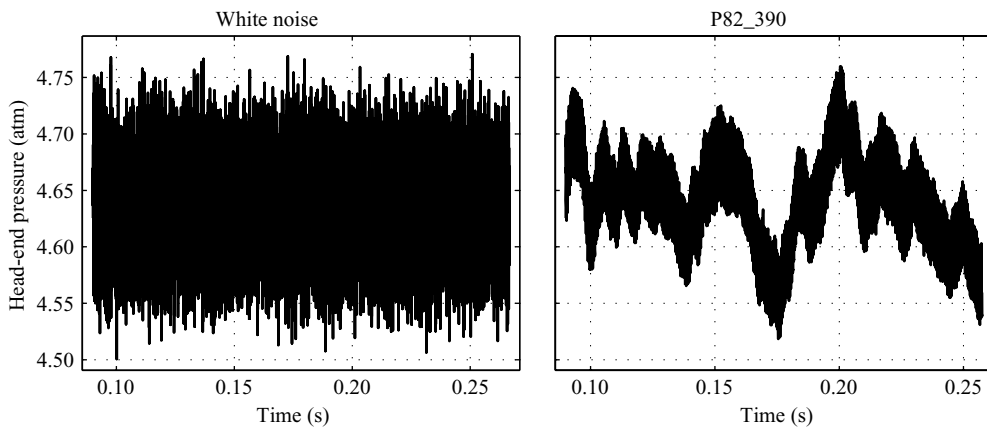
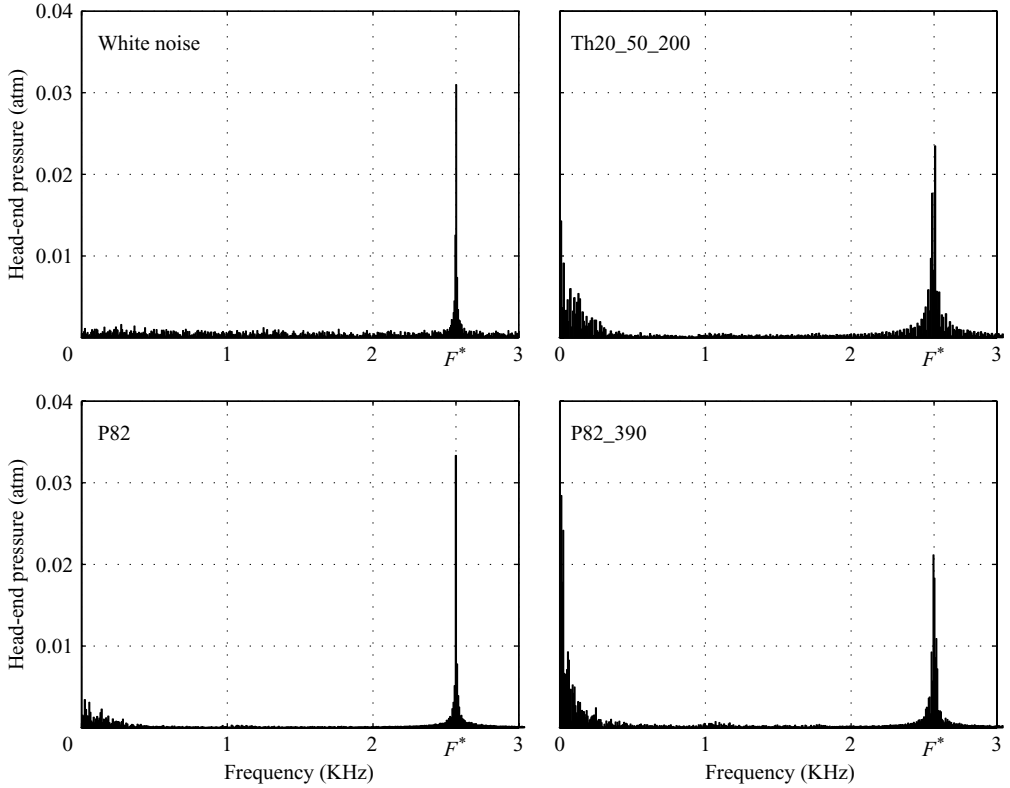


FIGURE 27. Comparison of head-end pressure time traces for the OneraC1 rocket when the efflux is defined by white noise or by P82_390 fluctuations; the processes have marginal p.d.f.s with identical means and standard deviations.

of surface-integrated quantities are overestimated. For this reason we cannot assume that the effects will be as large for a nominally axisymmetric (albeit three-dimensional) configuration. We hope to examine such configurations in the future.

Pack	Shedding frequency	$\frac{\sigma [P_{head}]}{\mu [P_{head}]} \times 100$	$\frac{\sigma [\dot{m}]}{\mu [\dot{m}]} \times 100$	$\frac{Cov[\dot{m} P_{head}]}{\sigma[\dot{m}]\sigma[P_{head}]}$
No fluctuations	2.54×10^3	0.5418	0	0
P82	2.54×10^3	0.5570	0.1	0.11
P82_390	2.54×10^3	0.9178	0.53	0.73
Th20_50_200	2.55×10^3	0.6500	0.62	0.40

TABLE 6. Results for the OneraC1 test case for three morphologies.

FIGURE 28. Panels from figures 25 and 26 in the frequency domain; F^* is the second axial mode frequency.

7. Concluding remarks

Our earlier work on heterogeneous propellant combustion (Massa *et al.* 2002, 2005) is, we believe, the only fully coupled three-dimensional treatment of this problem, and so the fluctuations above the propellant on the millimetre scale are described here for the first time. It is self-evident that the size of the AP particles plays a role in defining the spatial variations of these fluctuations, but we have found that surface clustering of the AP can define significantly longer length scales. However, for all but micro-rockets these will be much shorter than any relevant to, or that can be accommodated by, the chamber-flow calculations. Whether or not these subgrid scales can affect the chamber flow is an open question.

The same cannot be said of the temporal fluctuations. The p.d.f.s of these are approximately normally distributed, and the correlations affect the chamber flow, most noticeably the head-end pressure. The usual way of accounting for injection fluctuations is to model them using a white-noise process, but our calculations permit the specification of more realistic data, and there are significant differences, as figure 21 makes clear.

The obvious concern that we have already identified in § 5 is that the chamber flows we have calculated are all strictly two-dimensional, and so the question of whether propellant morphology can affect head-end pressure fluctuations in real rockets is not yet definitively answered. But that we obtain an effect within our restricted framework encourages us to pursue the more difficult real problem.

This work was supported by the US Department of Energy through the University of California under subcontract B341494, and by AFRL under contract FA9550-05-1-0029 and contract FA9550-06-C-0078.

REFERENCES

- BALACHANDAR, S., BUCKMASTER, J. & SHORT, M. 2001 The generation of axial vorticity in solid-propellant rocket-motor flows. *J. Fluid Mech.* **429**, 283–305.
- BALAKRISHNAN, G., LINAN, A. & WILLIAMS, F. A. 1991 Compressibility effects in thin channels with injection. *AIAA J.* **29** (12), 2149–2154.
- BECKSTEAD, M. W., DERR, R. L. & PRICE, C. F. 1970 A model of composite solid-propellant combustion based on multiple flames. *AIAA J.* **8** (12), 2200–2207.
- BOX, G. E. P. & MULLER, M. E. 1958 A note on the generation of random normal deviates. *Ann. Math. Statist.* **29**, 610–611.
- BREWSTER, M. Q. 2000 Solid propellant combustion response: quasi steady (QSHOD) theory development and validation. In *Solid Propellant Chemistry, Combustion and Motor Interior Ballistics* (ed. V. Yang, T. Brill & W.-Z. Ren), Vol. 185, pp. 607–637. AIAA.
- BUCKMASTER, J., JACKSON, T. L., MASSA, L. & ULRICH, M. 2005 Response of a burning heterogeneous propellant to small pressure disturbances. *Proc. Combust. Inst.* **30**, 2079–2086.
- CHEN, M., BUCKMASTER, J., JACKSON, T. L. & MASSA, L. 2002 Homogenization issues and the combustion of heterogeneous solid propellants. *Proc. Combust. Inst.* **29**, 2923–2929.
- CULICK, F. C. E. 1966 Rotational axisymmetric mean flow and damping of acoustic waves in solid propellant rocket motors. *AIAA J.* **4**, 1462–1464.
- FIEDLER, R., HASELBACHER, A., BREITENFELD, M., ALEXANDER, P., MASSA, L. & ROSS, W. 2005 3-D simulations of ignition transients in the RSRM. *AIAA Paper* 2005-3993.
- FIEDLER, R., WASISTO, B. & BRANDYBERRY, M. 2006 Full 3-D simulation of turbulent flow in the RSRM. *AIAA Paper* 2006-4587.
- FLANDRO, G. 1986 Vortex driving mechanism in oscillatory rocket flows. *J. Propul. Power* **2** (3), 206–214.
- JACKSON, T. L. & BUCKMASTER, J. 2002 Heterogeneous propellant combustion. *AIAA J.* **40** (6), 1122–1130.
- KNOTT, G. M., JACKSON, T. L. & BUCKMASTER, J. 2001 The random packing of heterogeneous propellants. *AIAA J.* **39**, 678–686.
- KOCHEVETS, S., BUCKMASTER, J., JACKSON, T. L. & HEGAB, A. 2001 Random packs and their use in the modeling of heterogeneous solid propellant combustion. *J. Propul. Power* **17**, 883–891.
- KOUTA, A. 1999 Computation of vortex shedding in solid rocket motors using a time-dependent turbulence model. *J. Propul. Power* **15** (3), 390–400.
- LANDSBAUM, E. 2005 Erosive burning of solid rocket propellants – a revisit. *J. Propul. Power* **21** (3), 470–477.
- LUPOGLAZOFF, M. & VUILLOT, F. 1992 Numerical simulation of vortex shedding phenomenon in 2D test case solid rocket motors. *AIAA Paper* 92-0776.
- MASSA, L., JACKSON, T. L. & BUCKMASTER, J. 2005 New kinetics for a model of heterogeneous propellant combustion. *J. Propul. Power* **21** (5), 914–924.

- MASSA, L., JACKSON, T. L., BUCKMASTER, J. & CAMPBELL, M. 2002 Three-dimensional heterogeneous propellant combustion. *Proc. Combust. Inst.* **29**, 2975–2983.
- MASSA, L., JACKSON, T. L. & SHORT, M. 2003 Numerical solution of three-dimensional heterogeneous solid propellants. *Combust. Theor. Modell.* **7**, 579–602.
- MILLER, R. R. 1982 Effects of particle size on reduced smoke propellant ballistics. *AIAA Paper* 82-1096.
- MOSER, R., ROGERS, M. & EWING, D. 1998 Self-similarity of time-evolving plane wakes. *J. Fluid Mech.* **367**, 255–289.
- PROUDMAN, I. 1962 An example of steady laminar flow at large Reynolds number. *J. Fluid Mech.* **9**, 593–502.
- SAMBAMURTHI, J., PRICE, E. & SIGMAN, R. 1984 Aluminum agglomeration in solid-propellant combustion. *AIAA J.* **22** (8), 1132–1138.
- TAYLOR, G. I. 1956 Fluid flow in regions bounded by porous surfaces. *Proc. R. Soc. Lond. A* **234**, 456–475.
- TENNEKES, H. & LUMLEY, J. 1972 *A First Course in Turbulence*. MIT Press.
- TRAIANEAU, J., HERVAT, C. & KUENTZMANN, P. 1986 Cold-flow simulation of a two-dimensional nozzleless solid rocket motor. *AIAA Paper* 86-1447.
- WANG, X. & JACKSON, T. L. 2005 The numerical simulation of two-dimensional aluminized composite solid propellant combustion. *Combust. Theor. Modell.* **9**, 171–197.
- WANG, X., JACKSON, T. L. & BUCKMASTER, J. 2007a Numerical simulation of the three-dimensional combustion of aluminized heterogeneous propellants. *Proc. Combust. Inst.* **31**, in press.
- WANG, X., JACKSON, T. L. & BUCKMASTER, J. 2007b The burning of ammonium-perchlorate ellipses and spheroids in fuel binder. *J. of Propulsion Power*, in press.
- WASISTO, B., BALACHANDAR, S. & MOSER, R. D. 2004 Compressible wall-injection flows in laminar, transitional, and turbulent regimes: numerical prediction. *J. Spacecraft Rockets* **41** (6), 915–924.
- WASISTO, B. & MOSER, R. D. 2005 Simulation strategy of turbulent internal flow in solid rocket motor. *J. Propul. Power* **21** (2) 251–263.
- ZHAO, Q., STAAB, P., KASSOY, D. & KIRKKOPRU, K. 2000 Acoustically generated vorticity in an internal flow. *J. Fluid Mech.* **413**, 247–285.

Reproduced with permission of the copyright owner. Further reproduction prohibited without permission.